



Supplementary Materials for

Dual-initiation ruptures in the 2024 Noto earthquake encircling a fault asperity at a swarm edge

Liuwei Xu *et al.*

Corresponding authors: Chen Ji, ji@geol.ucsb.edu; Lingsen Meng, lsmeng@g.ucla.edu

Science **385**, 871 (2024)
DOI: 10.1126/science.adp0493

The PDF file includes:

Materials and Methods
Figs. S1 to S26
Tables S1 to S7
References

Other Supplementary Material for this manuscript includes the following:

Movies S1 to S5

Materials and Methods

Slowness-Enhanced Back-Projection

The Back-Projection (BP) technique tracks the propagation of earthquake rupture fronts based on coherent seismic recordings from dense networks of seismometers (57, 58, 59). Our Slowness-Enhanced Back-Projection (SEBP) analysis adopts the method developed by (14) and (15), enhancing the accuracy and resolution of rupture front locating compared to standard BP. We collect P waveforms recorded by arrays in Alaska (147 stations), Australia (129 stations), US (468 stations), and Europe (233 stations). For each array, waveforms are downloaded and manually aligned based on P arrivals, which ensures that the first arrival on observed seismograms comes from the hypocenter location. The aligned waveforms are bandpass filtered between 0.5-2 Hz, which enables high-resolution while guaranteeing a high enough signal to noise ratio. The above alignment corrects the travel time error caused by the deviation of Earth's 3D structure from the 1D reference model, and enables the spatial accuracy of resolved high-frequency (HF) radiators. However, it is only valid in the vicinity of the hypocenter and becomes less effective as the rupture propagates further away. To accurately capture and mitigate travel time errors in the entire source region, our method utilizes 3 to 7 aftershocks spanning along the rupture path (table S2) to derive the slowness correction terms for all arrays (figs. S1-S4). These correction terms are then applied to the mainshock BP to calibrate the travel time errors. With the slowness calibrations, the root mean square of the distance between the BP inferred aftershock locations and the JMA catalog locations reduces from ~9 km to ~ 3 km (table S2), indicating that BP analysis suffers less from the travel time errors and provides a better depiction of the rupture process (Fig. 1, figs. S1-S4).

The BP radiators' spatial distribution is depicted in Fig. 1 and figs. S1-S4. To obtain the rupture speeds shown in Fig. 2, we calculate the BP radiators' along-fault distances while accounting for the strike changes in the fault model of Fig. 4B. The calculations are as follows:

For BP radiators inside segment 1:

$$\text{Along-fault distance} = \text{epicenter distance} * \cos[\text{radiator's azimuth (relative to the epicenter)} - \text{segment 1 azimuth}]$$

For BP radiators inside segment 2:

$$\text{Along-fault distance} = \text{distance to the top-west corner of segment 1} * \cos[\text{radiator's azimuth (relative to the top-west of segment 1)} - \text{segment 2 azimuth}] + \text{southwest branch length of segment 1}$$

For BP radiators inside segment 3:

$$\text{Along-fault distance} = \text{distance to the top-east corner of segment 1} * \cos[\text{radiator's azimuth (relative to the top-east segment 1)} - \text{segment 3 azimuth}] + \text{norotheast branch length of segment 1}$$

We use positive values to indicate distances to the NE and negative values to the SW. To determine the rupture speed, we merge BP radiators from all arrays into one file, calculate all radiators' along-fault distances, and identify the leading radiators (the radiators with the furthest along-fault distance at each time) for the early rupture stage (first 16 s), the NE branch, and the SW branch.

The linearly-fitted rupture speeds are 0.79 km/s for the early stage, 2.38 km/s for the SW branch, and 2.06 km/s for the NE branch, respectively.

Joint Finite Fault Inversion

The Finite Fault Inversion (FFI) method could resolve the slip amplitude, slip rate, and rupture progression on earthquake faults. We use the joint FFI developed by (16) and (17) and include 15 3-component recordings at near-fault K-net and KiK-net strong motion stations (49) (vertical-Z, radial-R, transverse-T; bandpass filtered to 0.025–0.3 Hz, figs. S15 and S9), 36 broadband teleseismic P waves (bandpass filtered to 2–333 s, figs. S16 and S17), 21 broadband teleseismic S waves (bandpass filtered to 2–333 s, figs. S16 and S17), 37 long-period teleseismic Rayleigh waves (bandpass filtered to 166–250 s, figs. S18 and S19), 20 long-period teleseismic Love waves (bandpass filtered to 166–250 s, figs. S18 and S19). The joint FFI also incorporates geodetic data to better constrain the slip amplitude. We derive static ground displacements from ALOS-2 SAR (fig. S20) and GNSS data (fig. S21). The weights of all datasets are listed in table S3. For this study, to emphasize the fitting to the close stations, we especially weight ISK001, ISK002 nine times more than other strong motion stations, and weight ISKH01 nineteen times more than other stations.

For each subfault, we invert slip amplitude, rake angle, rupture initiation time, and the shape of the asymmetric slip rate function. Detailed equations and algorithms are described in (16, 17). The seismic data are transformed into wavelet domains to simultaneously capture the characteristics in the high-frequency and low-frequency and preserve the information in the time-domain. The misfits for static ground deformation measured by SAR and GNSS are calculated separately: We use the weighted sum-squared residuals to quantify the difference between observed and modeled data (60). The weights are inversely proportional to the standard deviation at each data point.

We identify the fault planes based on the aftershock distribution. We collect the locations of aftershocks that occurred during Jan 1, 2024 to Jan 21, 2024 from the JMA catalog (Fig. 1). Three fault planes (segments 1–3 in Fig. 4) are set to model the rupture. Segments 1 and 2 dip toward the southeast and Segment 3 dips towards the northwest (Fig. 3A, B; table S4). The dipping directions and angles match the aftershock distribution (Fig. 3A, B). Considering the potential uncertainty in fault geometry, we conduct five inversions, using the dip angle of 32, 36, 40, 42, 46 degrees for segment 1. We calculate the normalized residual for all inversions, defined as [(residual of each inversion - minimum residual of all inversions) / minimum residual of all inversions]. Residuals for seismic, GNSS, and SAR data are computed, and the model with the minimum sum of normalized residuals is chosen as the preferred one (40 degree, fig. S22, table S4). We parameterize the fault planes with 56 and 16 subfaults in the along strike and dip directions, respectively. The subfault size is 3 km (along strike) by 2 km (downdip; Fig. 4A). The hypocenter is set at 37.518°N, 137.242°E, 10.07 km depth (JMA catalog, accessed on Jan 12). The rupture velocity is allowed between 0.1 km/s to 3.5 km/s with a reference speed of 1.5 km/s, and the rake angle is allowed $\pm 40^\circ$ from the reference angle of 112°. The lower boundary of the rupture velocity (~0.1 km/s) is required by the vertical displacement at station ISKH01 (Fig. 5C). Note that this record suggests that the fault patch in the vicinity of this station did not fail until ~20 s. We allow

the starting time and ending time of the asymmetric slip rate function (17) to change from 0.4 to 6.0 s. We stabilize the inversions by applying two constraints: to reduce the difference between the slip on adjacent subfaults and to reduce the total seismic moment (16, 61). Green's functions for local strong motion waveforms and static displacements are computed using the f-k integration approach by (62) and the 1-D crust model by (63) (table. S5).

The distributions of the selected strong motion stations and geodetic measurements are mainly concentrated in the Noto Peninsula, limiting the spatiotemporal resolution of the inverted fault model. To explore the model's uncertainty in the offshore part of Segment 1 and Segment 3, we conduct two additional inversions. Compared with the preferred model, the northeast branch of Segment 1 of the first additional model is extended by 12 km (the “extended model”, fig. S23), and the second additional model has a flatter Segment 3 (25° , the “flatter model”, fig. S24). The results are shown in figs. S23 & S24. In comparison with the preferred model, these two models have nearly identical moment magnitude and moment rate functions for Segments 1 and 3 (fig. S25), but notably different slip distributions on Segment 3 and the eastern end of Segment 1. However, the uncertainty near the eastern end of the fault does not affect the dual-initiation rupture process near the hypocenter (figs. S23 & S24).

Grid Search for the Best-fit Second Hypocenter Location

To pinpoint the optimal location of the second hypocenter, we initiate the process by identifying the arrival time of the S wave (T_2) within the second wave cluster. Given the dominance of S waves in the near-field and their clearer identification, we manually picked T_2 from vertical acceleration seismograms (Fig. 5, fig. S10). We further compute two time-series datasets to validate the manual picking:

1. The square root of the sum of squares of the East-West (A_e), North-South (A_n), and Up-Down (A_u) velocity seismograms: $[(A_e^2 + A_n^2 + A_u^2)^{0.5}]$. All waveforms are bandpass filtered within the range of 0.2 to 5 Hz (fig. S11A, C, E, G, I, K).
2. The ratio of the sum of squares of A_e and A_n to the total sum of squares, adjusted by a small constant: $[(A_e^2 + A_n^2) / (A_e^2 + A_n^2 + A_u^2 + 0.0001 * \max(A_e^2 + A_n^2 + A_u^2))]$. This ratio emphasizes the larger horizontal components in the waveform (fig. S11B, D, F, H, J, L).

In essence, if the S wave arrives at T_2 , we anticipate observing rising amplitudes in dataset 1 and dataset 2. Our observation in fig S11 is consistent with the above expectation. The picked T_2 ($T_2\text{-ISK}^*$) for each station is listed in table S6.

Next, we calculate each station's T_2 difference with respect to ISK001:

$$\begin{aligned} T_{\text{obsdiff}}\text{-ISKH01} &= (T_2\text{-ISKH01} - T_2\text{-ISK001}), \\ T_{\text{obsdiff}}\text{-ISKH02} &= (T_2\text{-ISKH02} - T_2\text{-ISK001}), \\ T_{\text{obsdiff}}\text{-ISKH03} &= (T_2\text{-ISKH03} - T_2\text{-ISK001}). \end{aligned}$$

$$\begin{aligned} T_{\text{obsdiff}}\text{-ISK002} &= (T_2\text{-ISK002} - T_2\text{-ISK001}), \\ T_{\text{obsdiff}}\text{-ISK003} &= (T_2\text{-ISK003} - T_2\text{-ISK001}), \end{aligned}$$

Then, we perform a grid-search within specified latitude (37.4:0.01:37.5), longitude (136.98:0.01:137.20), and depth (3:1:15 km) ranges. For each grid point, we compute the S-wave travel time predictions for all stations ($T_{\text{pre_ISKH01}}$, ISKH01 , ISKH02 , ISKH02 , ISKH03 , ISKH03). We compute the time difference between each station's prediction with respect to the ISKH01 :

$$\begin{aligned} T_{\text{prediff_ISKH01}} &= (T_{\text{pre_ISKH01}} - T_{\text{pre_ISKH01}}), & T_{\text{prediff_ISKH02}} &= (T_{\text{pre_ISKH02}} - T_{\text{pre_ISKH01}}), \\ T_{\text{prediff_ISKH02}} &= (T_{\text{pre_ISKH02}} - T_{\text{pre_ISKH01}}), & T_{\text{prediff_ISKH03}} &= (T_{\text{pre_ISKH03}} - T_{\text{pre_ISKH01}}), \\ T_{\text{prediff_ISKH03}} &= (T_{\text{pre_ISKH03}} - T_{\text{pre_ISKH01}}). \end{aligned}$$

By utilizing the time difference, we exclude the potential influence from the uncertainty of the second hypocenter onset time. The goal is to minimize the least-square misfit between the observations and predictions.

$$\begin{aligned} \text{Misfit} = & (T_{\text{obsdiff_ISKH01}} - T_{\text{prediff_ISKH01}})^2 + (T_{\text{obsdiff_ISKH02}} - T_{\text{prediff_ISKH02}})^2 + \\ & (T_{\text{obsdiff_ISKH02}} - T_{\text{prediff_ISKH02}})^2 + (T_{\text{obsdiff_ISKH03}} - T_{\text{prediff_ISKH03}})^2 + (T_{\text{obsdiff_ISKH03}} - \\ & T_{\text{prediff_ISKH03}})^2 \end{aligned}$$

The coordinates that yield the smallest misfit represent the best-fit location of the second hypocenter. We then use 10 s as the second hypocenter onset time and predict S arrivals based on the best-fit location (137.07°E, 37.48°N, 7 km depth). We plot predicted arrivals as purple dashed lines in Fig. 5, figs. S10-S11.

We also make an evaluation on the uncertainty of the second hypocenter. We adopt χ^2 uncertainty evaluation following (56). For a given hypocenter candidate $m = (\text{longitude}, \text{latitude}, \text{depth}, \text{time})$, $\chi^2(m)$ is defined as:

$$\chi^2(m) = \sum_{i=1}^n \frac{[t_i - t_i^p]^2}{\sigma^2(m_{\text{best}})} \quad (\text{eq 1})$$

where i is the station index, n is the total station number (in our case $n=6$), t_i is the picked time at station i , t_i^p is the predicted time at station i , $\sigma^2(m_{\text{best}})$ is the residuals at the best-fit hypocenter and is defined as:

$$\sigma^2(m_{\text{best}}) = \frac{\sum_{i=1}^n [t_i - t_i^p(m_{\text{best}})]^2}{n_{df}} \quad (\text{eq 2})$$

where n_{df} is the degrees of freedom (in our case $n_{df}=6-4=2$ because m has 4 components).

The value $\chi^2(m)$ will grow as we move away from the best-fitting hypocenter. We calculate the contour of the 95% confidence interval for the second hypocenter and plot it as a gray dashed line in Fig. 5G and figs. S8. There is only a 5% chance that the value of χ^2 will fall beyond the contour.

Synthetic Aperture Radar

Images from radar satellites can be used to extract the static coseismic ground deformation. We apply speckle tracking (also known as pixel tracking or amplitude cross-correlation) to three pairs of ALOS-2 SAR images acquired before and after the earthquake (see table S7 in the Supplementary Materials for detailed information) for the ground surface deformation in the slant range (radar line-of-sight, or cross-track) and ground azimuth (along-track) directions via the InSAR Scientific Computing Environment (ISCE) version 2 software (41) using the “alos2App.py” application (64) (fig. S26). For each pair, the two single look complex (SLC) data are coregistered with each other using precise orbits and GLO-30 Copernicus DEM (65). We use a cross-correlation window of 128 by 128 or 64 by 64 in range and azimuth directions, respectively, and then oversample the covariance surface by a factor of 64 for refinement. To further reduce the estimation noise, we mask out pixels on the water body, or with abnormally large estimation values (>5 m in the range direction; >6 m in the azimuth direction), or with abnormally large estimation standard deviations, or with abnormally small estimation signal-to-noise ratios (<5 dB). All estimations are geocoded to a grid in the size of 150 or 60 m.

Global Navigation Satellite System

The coseismic GNSS displacements are obtained from the Nevada Geodetic Laboratory (NGL), University of Nevada at Reno (66). Data recorded by Japan’s GNSS Earth Observation Network System (GEONET) are processed by NGL using GipsyX software (67) from Jet Propulsion Laboratory (JPL) based on JPL rapid orbit to obtain the 5-minute sample rate station position time series, which is then used to estimate the coseismic displacement and accessed in 2024-01-14 (fig. S21). To eliminate the effect of the Mw6.2 event, which occurred 8 minutes following the main shock, only data collected between the Mw7.5 and Mw6.2 events are used to constrain positions. The maximum displacement is at station JO53, which moves ~1.25 m horizontally and ~1.05 m vertically upward.

Stress Drop Calculation

For a given model m, the shear stress drop at the center of the (i, j) subfault can be calculated by:

$$\Delta\tau_{ij}^r(m) = \sum_{k=1}^N \sum_{l=1}^M [D_{kl}^1(m)\sigma_{ij,kl}^{r,1} + D_{kl}^2(m)\sigma_{ij,kl}^{r,2}], \quad (\text{eq } 3)$$

where $\Delta\tau_{ij}^r(m)$, for r=1,2, denotes the left-lateral (r=1) or thrust shear (r=2) stress at this location, respectively. $D_{kl}^P(m)$, for P=1,2, is the corresponding left-lateral (P=1) or thrust (P=2) slip at the (k,l) subfault. $\sigma_{ij,kl}^{r,P}$ is the kernel function representing the shear stress response at the center of subfault (i,j) caused by unit slip on subfault (k,l), which is calculated using Okada’s half-space equations (68). We scale the calculated kernel function with rigidity to approximately account for variations in shear wave velocity and density (69).

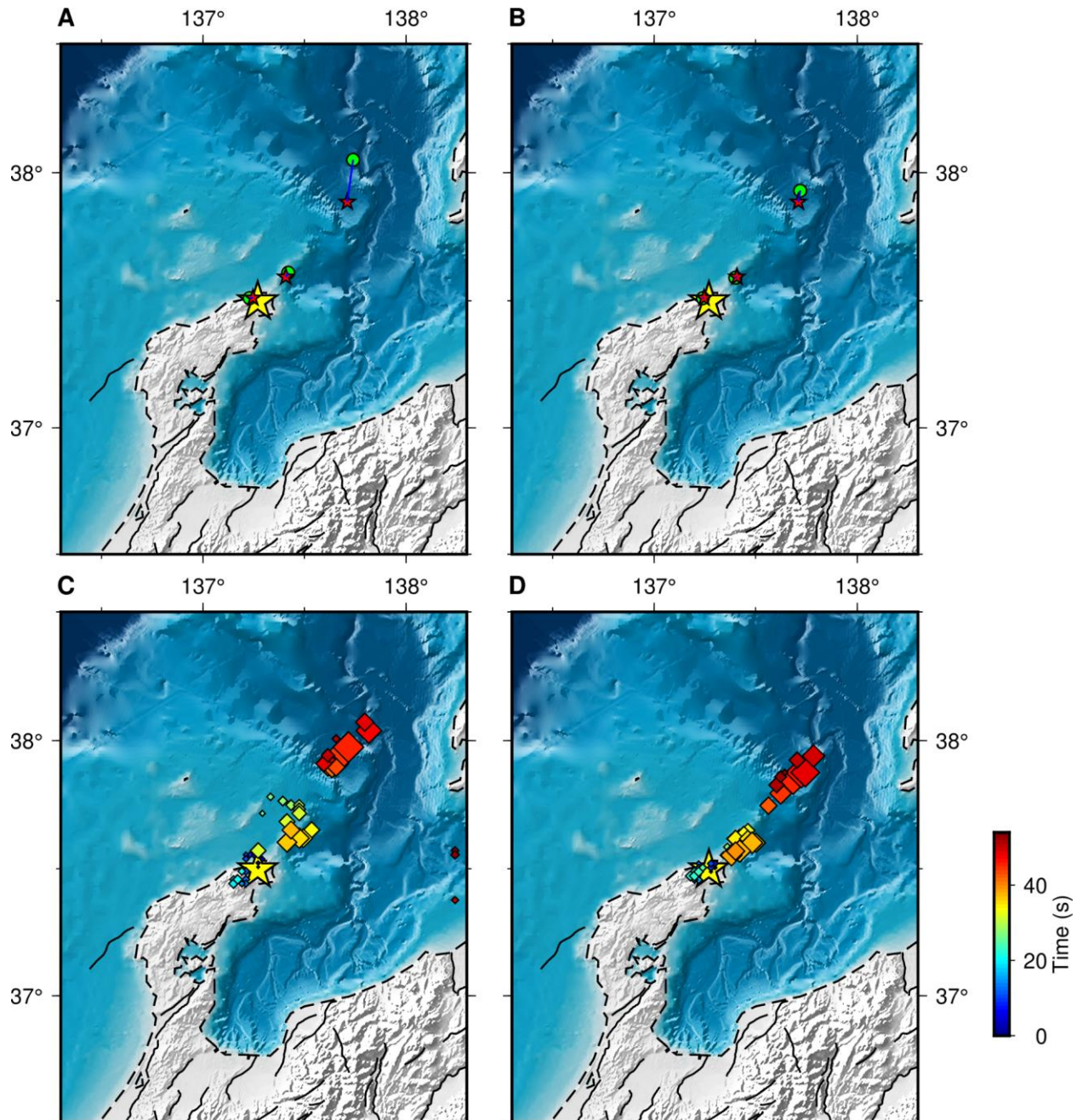


Fig. S1. Comparison of aftershock locations and mainshock BPs by the Alaska array before and after calibration. (A) The AK array's results for aftershocks along the rupture path before slowness calibration. (B) The AK array's results for aftershocks along the rupture path after slowness calibration. (C) The AK array's results for the mainshock before slowness calibration. (D) The AK array's results for the mainshock after slowness calibration. Green circles denote the BP-inferred locations of M5+ aftershocks spanning the rupture region. The red stars denote the JMA catalog epicenter of aftershocks. The yellow star denotes the epicenter of the mainshock. Diamonds denote the HF radiators for the Mw 7.5 event, color-coded by rupture time relative to the origin time of the event and with a size proportional to the normalized BP power.

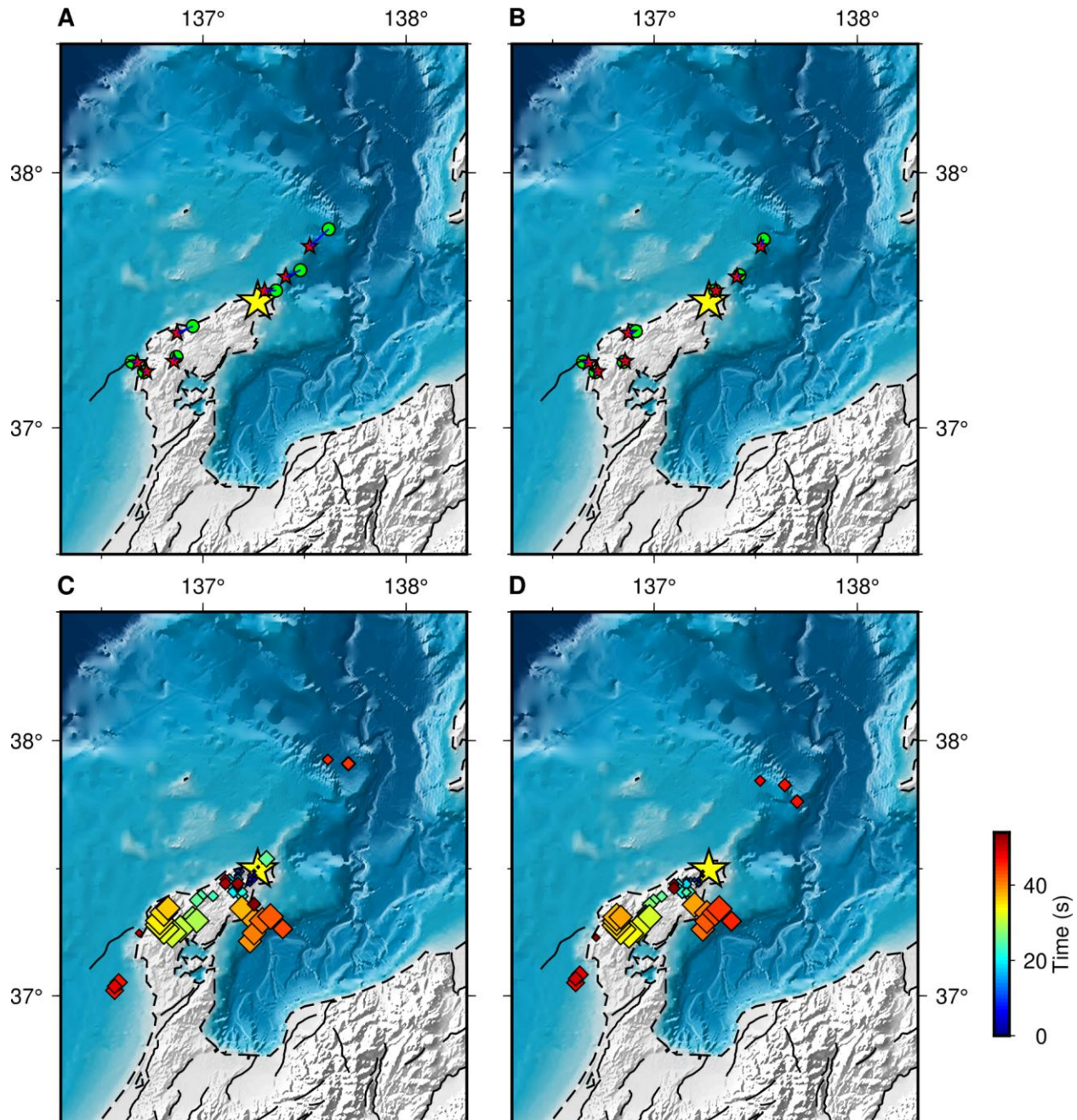


Fig. S2. Comparison of aftershock locations and mainshock BPs by the Australia array before and after calibration. (A) The AU array's results for aftershocks along the rupture path before slowness calibration. (B) The AU array's results for aftershocks along the rupture path after slowness calibration. (C) The AU array's results for the mainshock before slowness calibration. (D) The AU array's results for the mainshock after slowness calibration. Green circles denote the BP-inferred locations of M5+ aftershocks spanning the rupture region. The red stars denote the JMA catalog epicenter of aftershocks. The yellow star denotes the epicenter of the mainshock. Diamonds denote the HF radiators for the Mw 7.5 event, color-coded by rupture time relative to the origin time of the event and with a size proportional to the normalized BP power.

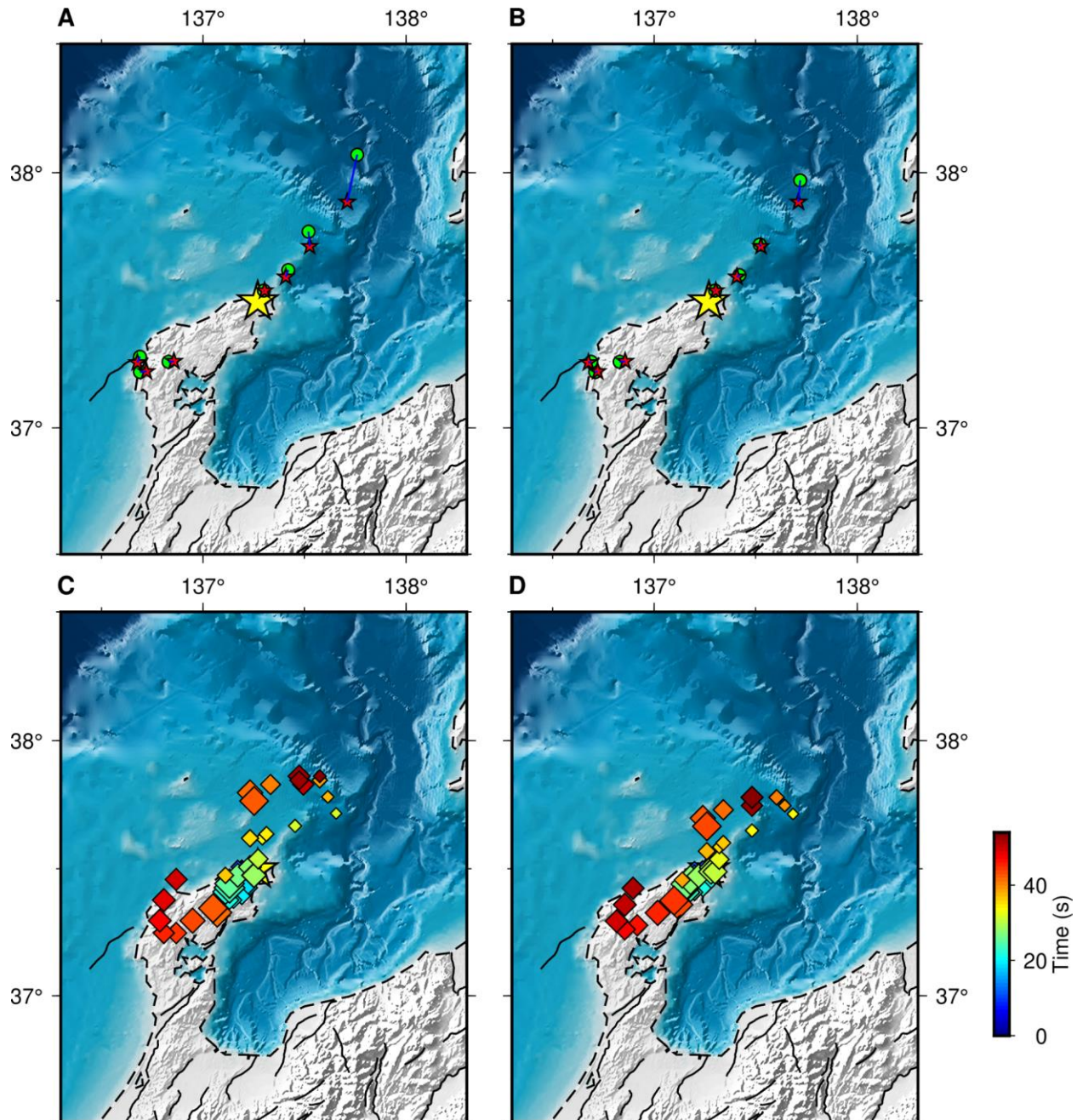


Fig. S3. Comparison of aftershock locations and mainshock BPs by the Europe array before and after calibration. (A) The EU array's results for aftershocks along the rupture path before slowness calibration. (B) The EU array's results for aftershocks along the rupture path after slowness calibration. (C) The EU array's results for the mainshock before slowness calibration. (D) The EU array's results for the mainshock after slowness calibration. Green circles denote the BP-inferred locations of M5+ aftershocks spanning the rupture region. The red stars denote the JMA catalog epicenter of aftershocks. The yellow star denotes the epicenter of the mainshock. Diamonds denote the HF radiators for the Mw 7.5 event, color-coded by rupture time relative to the origin time of the event and with a size proportional to the normalized BP power.

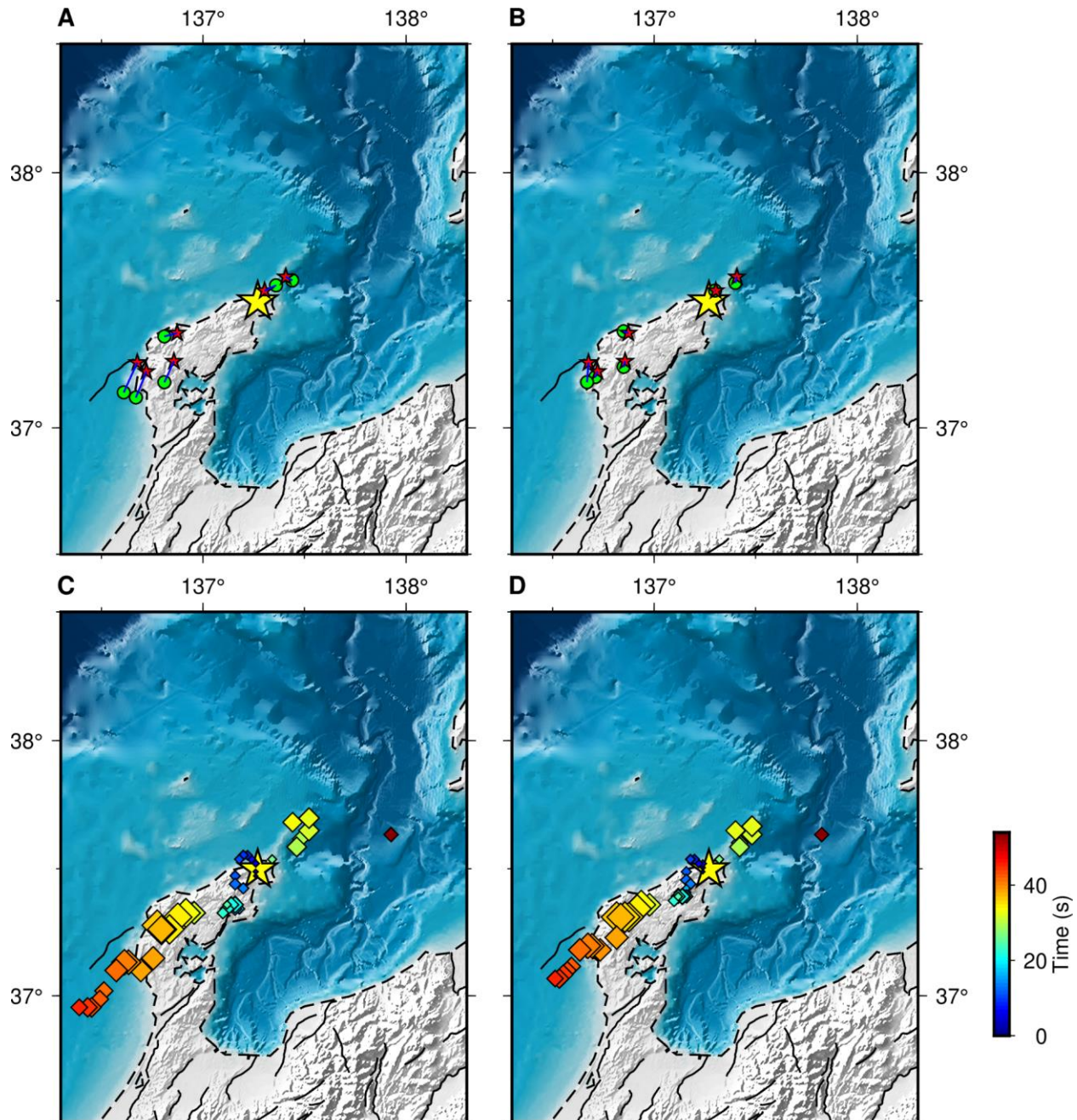


Fig. S4. Comparison of aftershock locations and mainshock BPs by the USArray before and after calibration. (A) The USArray’s results for aftershocks along the rupture path before slowness calibration. (B) The USArray’s results for aftershocks along the rupture path after slowness calibration. (C) The USArray’s results for the mainshock before slowness calibration. (D) The USArray’s results for the mainshock after slowness calibration. Green circles denote the BP-inferred locations of M5+ aftershocks spanning the rupture region. The red stars denote the JMA catalog epicenter of aftershocks. The yellow star denotes the epicenter of the mainshock. Diamonds denote the HF radiators for the Mw 7.5 event, color-coded by rupture time relative to the origin time of the event and with a size proportional to the normalized BP power.

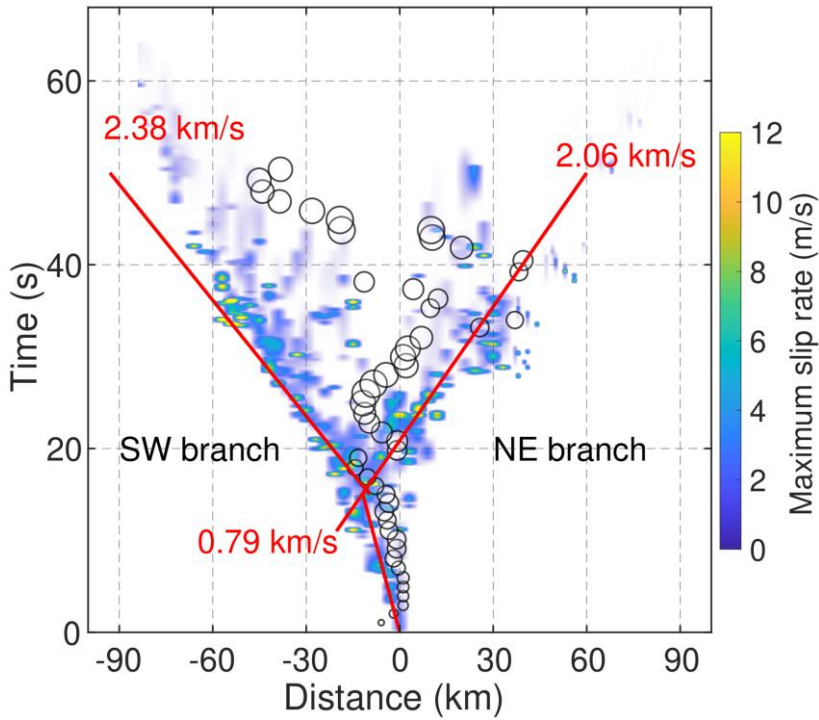


Fig. S5. SEBP results resolved by the Europe array. Circles indicate the location and timing of high-frequency radiators. Location is defined as the along-fault position relative to the hypocenter, positive to the northeast and negative to the southwest, accounting for the strike changes in the fault model of Fig. 4B. The red solid line shows the fitted steady rupture front in Fig. 2A, with average rupture speed indicated in red label. Background colormap indicates the maximum slip rate among all depths from FFI.

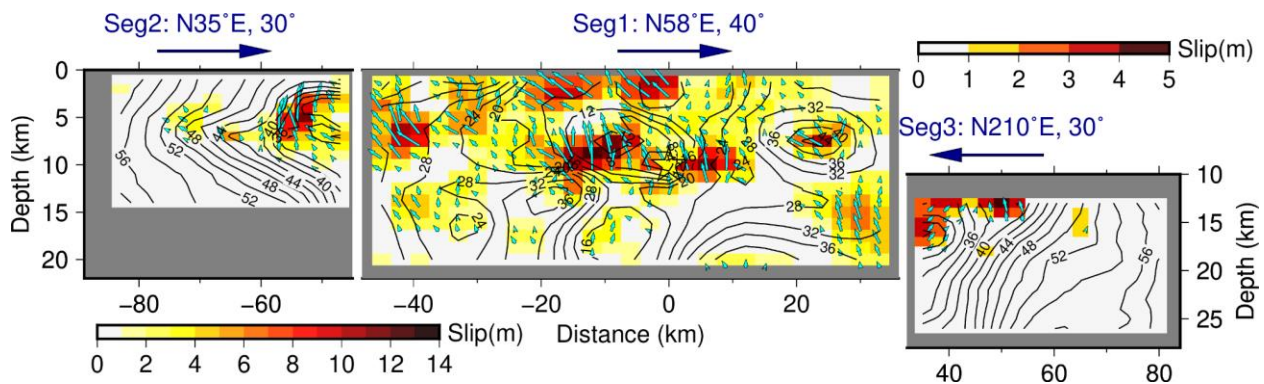
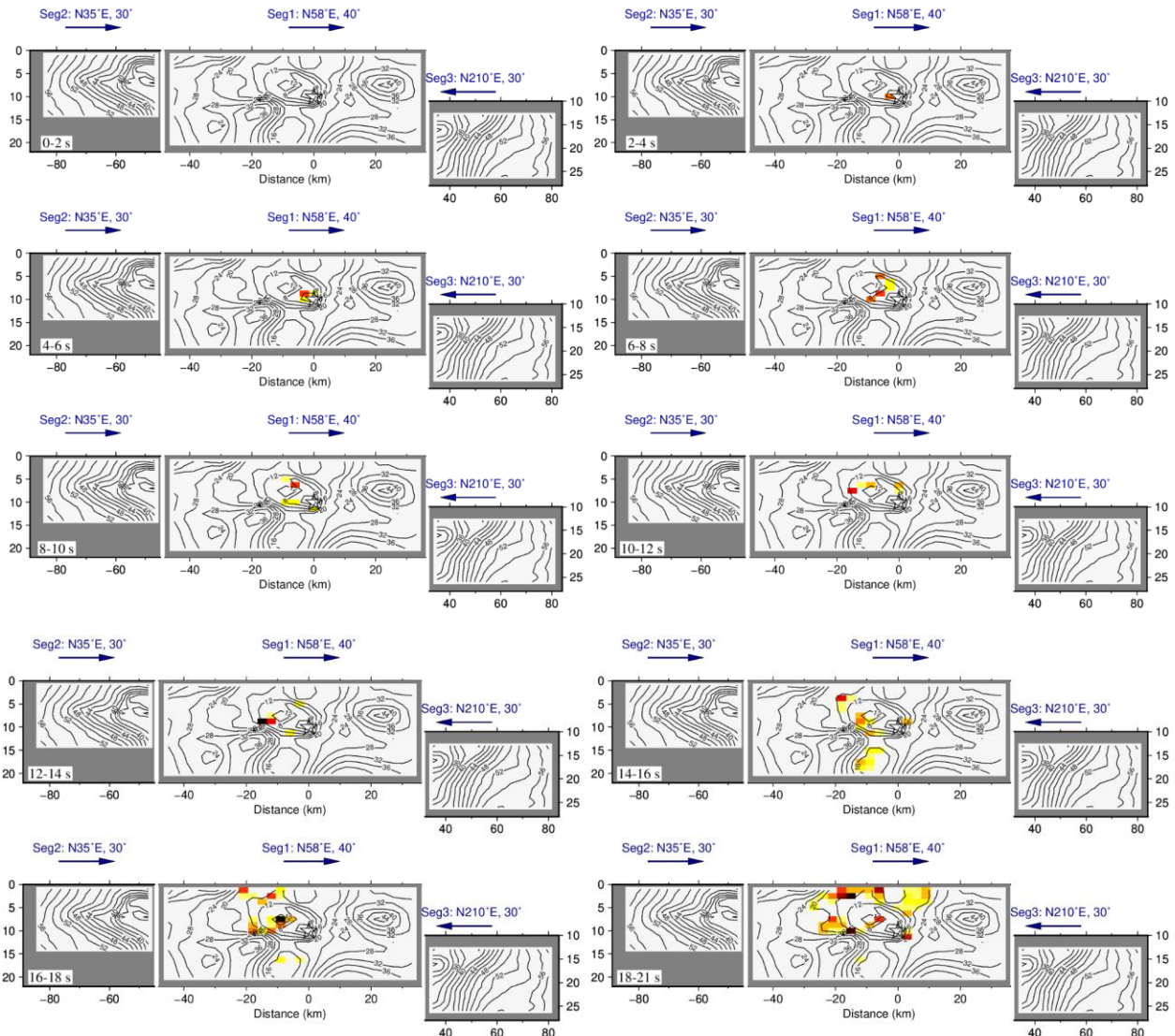


Fig. S6. Spatial distribution of final slip (colors), rupture initiation time (contours), and slip direction (rake angle, cyan arrows) of the preferred model. Top labels indicate the orientation (strike angle) and dip angle of each fault segment. The colorbar on the lower-left is the legend for slip on segments 1 and 2, and the colorbar on the upper-right is the legend for slip on segment 3.



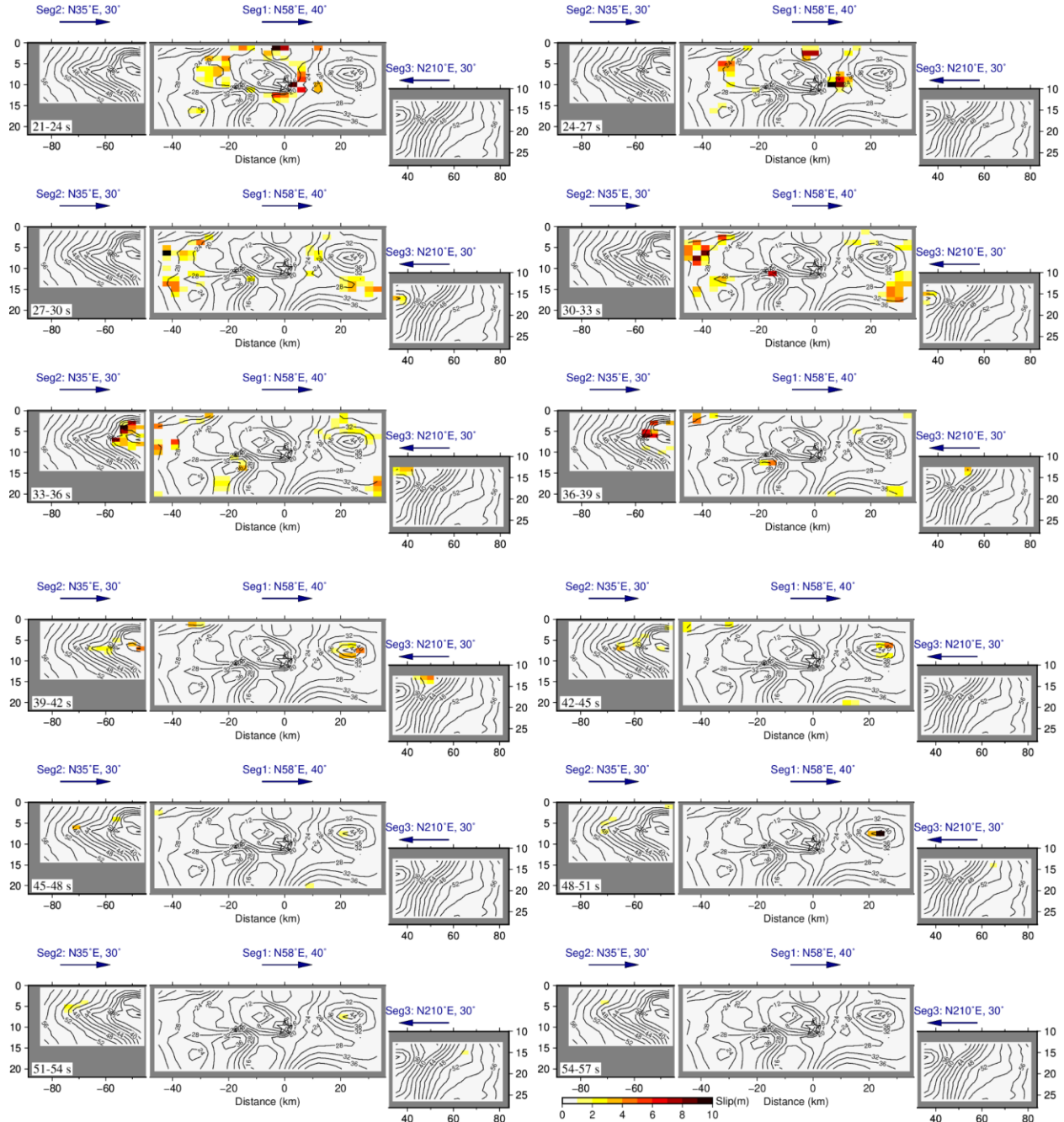


Fig. S7. Snapshots of the preferred FFI model at 2 s (before 18 s) and 3 s (after 18 s) time intervals. Time intervals are indicated at the lower left corner of each snapshot. The white star shows the hypocenter and the hot colorbar shows the slip in each time window.

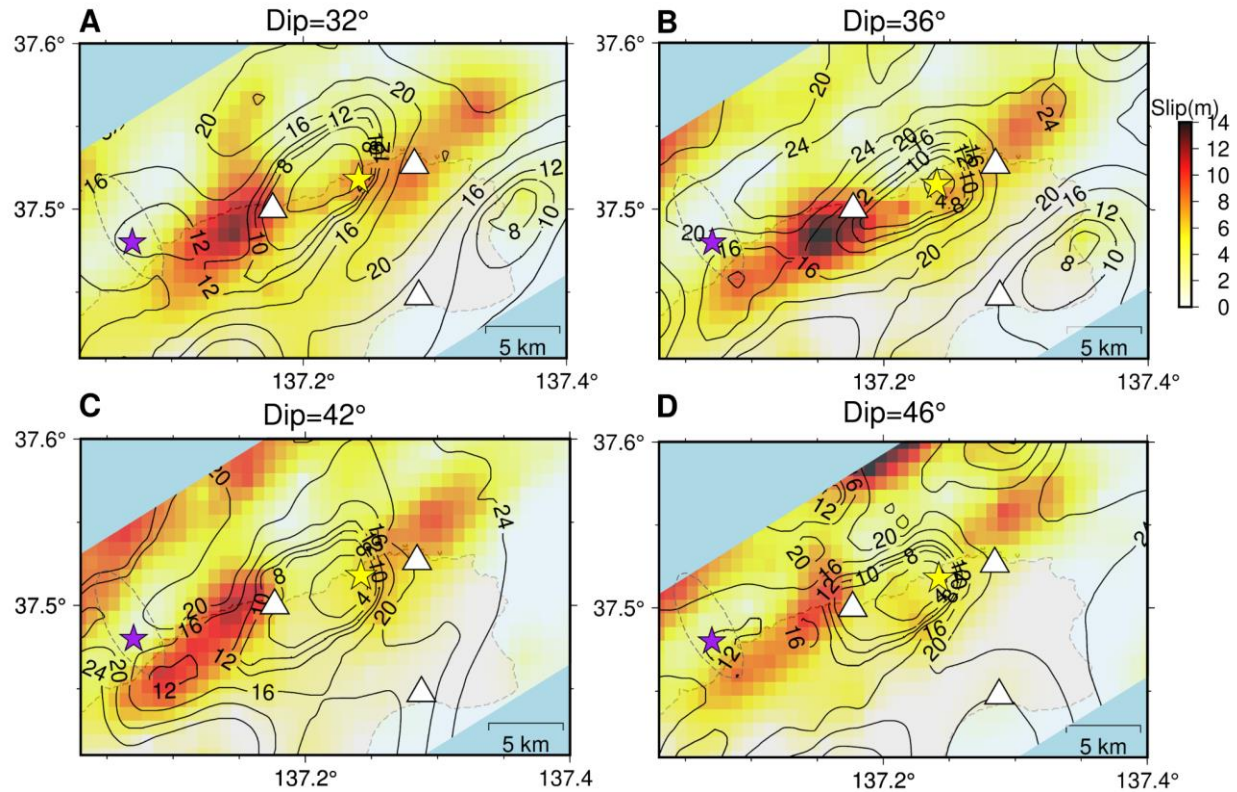


Fig. S8. Sketch of the early rupture stage for segment 1 with dip angles of 32° (A), 36° (B), 42° (C), and 46° (D). The yellow star denotes the hypocenter (Hypo-I) and the purple star denotes the second hypocenter (Hypo-II). The gray dashed contour around Hypo-II indicates the 95% confidence interval in χ^2 uncertainty evaluation (18, 56). The black contours and numbers denote the rupture time in seconds.

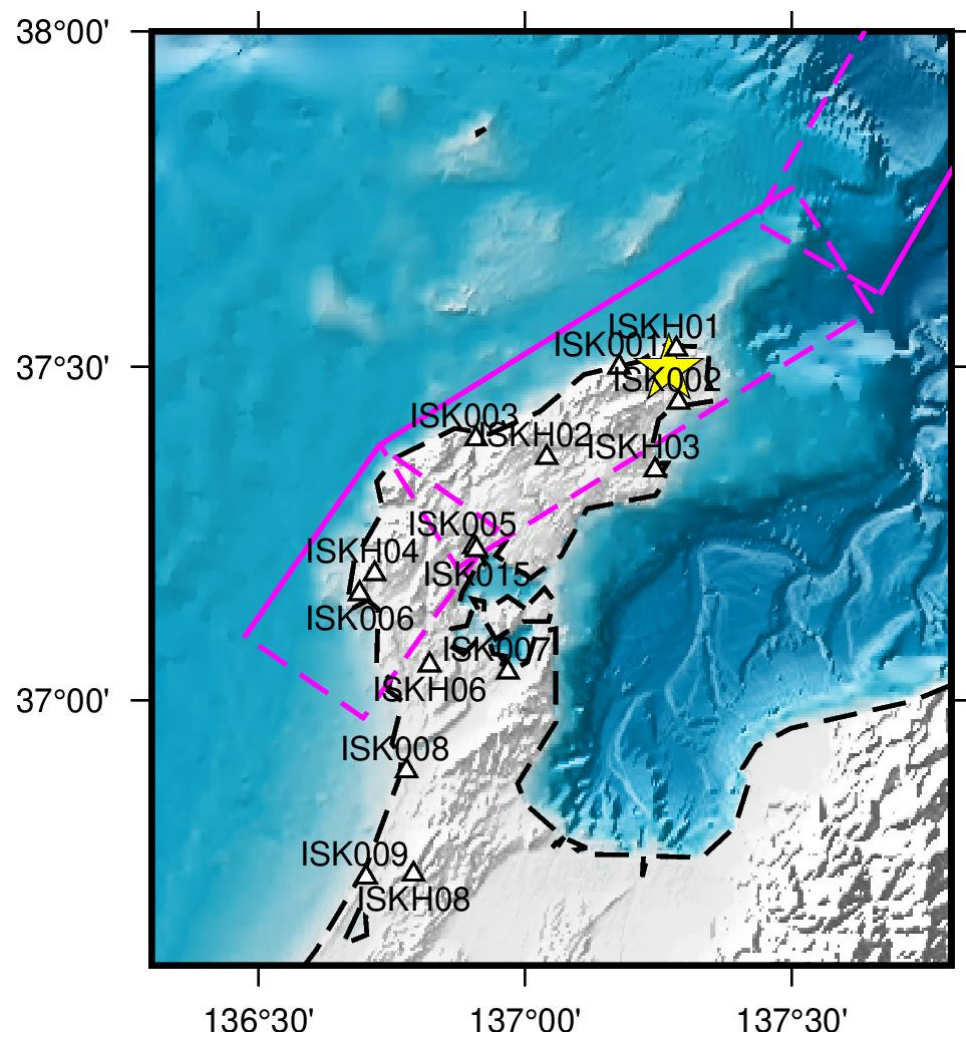


Fig. S9. The strong motion stations used in this study, with corresponding names. The magenta boxes denote the fault planes adopted in our finite fault inversion, with the solid magenta lines indicating their upper boundaries.

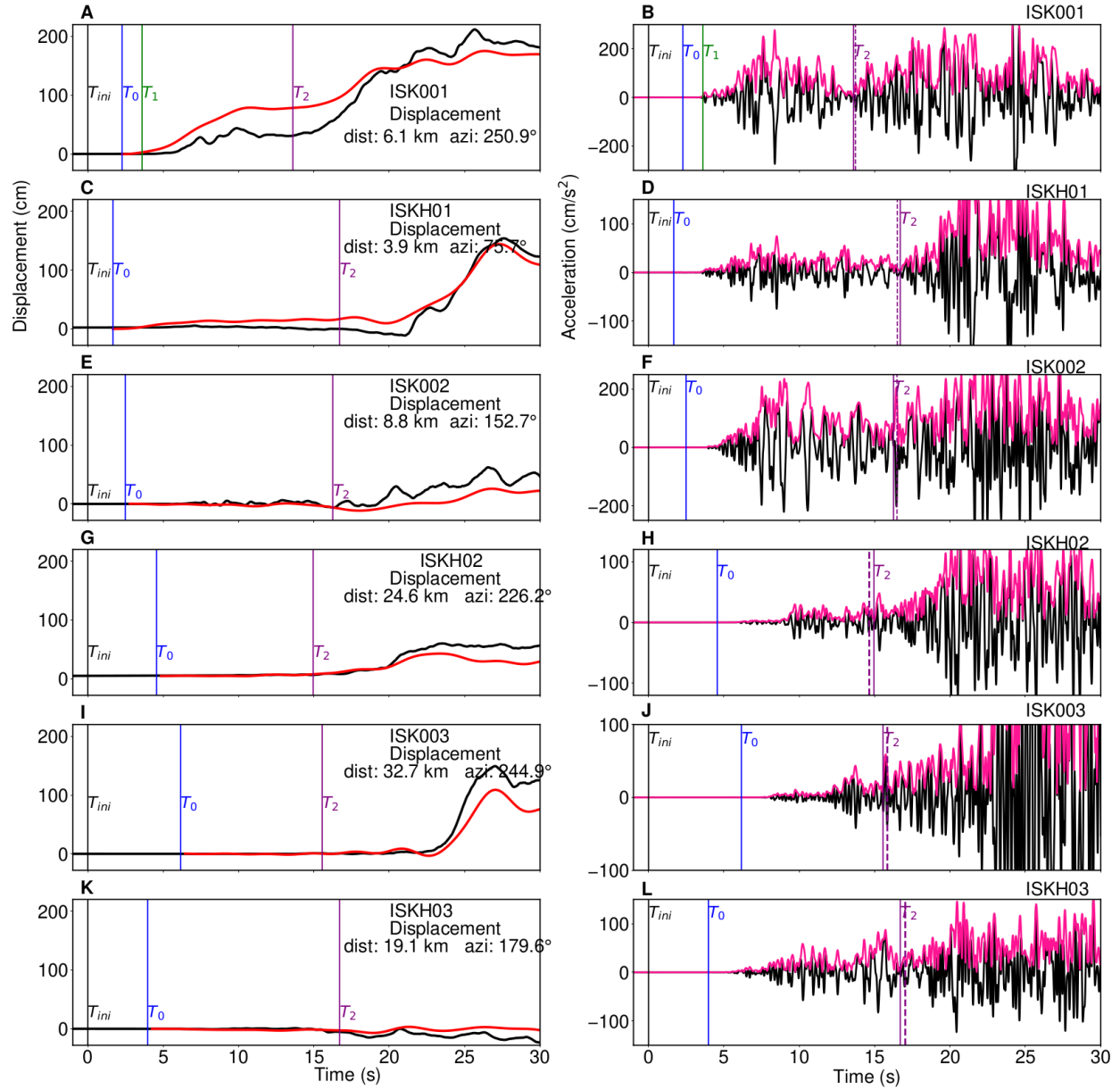


Fig. S10. Strong motion recordings from near-source stations. (A) Vertical displacement (black line) obtained by integrating acceleration recording and removing the drift (21) at station ISK001. The red line denotes the predicted waveform by the preferred FFI model. T_{ini} indicates the earthquake starting time, according to JMA catalog. T_0 is the manually picked P arrival, based on the acceleration seismogram (B). T_1 is the manually picked beginning of the first wave group, based on the acceleration seismogram (B). T_2 with the solid purple line is the manually picked beginning of the second wave group, based on the acceleration seismogram (B). The relative distance and azimuth from the hypocenter to the station are noted on the right. (B) Vertical acceleration seismogram recorded at station ISK001, bandpass filtered between 0.2–5 Hz. The pink line denotes the envelope of the waveform. The dashed purple line is the predicted S arrival time based on the best-fit second hypocenter location. (C,D) The same as (A,B) but for station ISKH01.

(E,F) The same as (A,B) but for station ISK002. (G,H) The same as (A,B) but for station ISKH02.
(I,J) The same as (A,B) but for station ISK003. (K,L) The same as (A,B) but for station ISKH03.

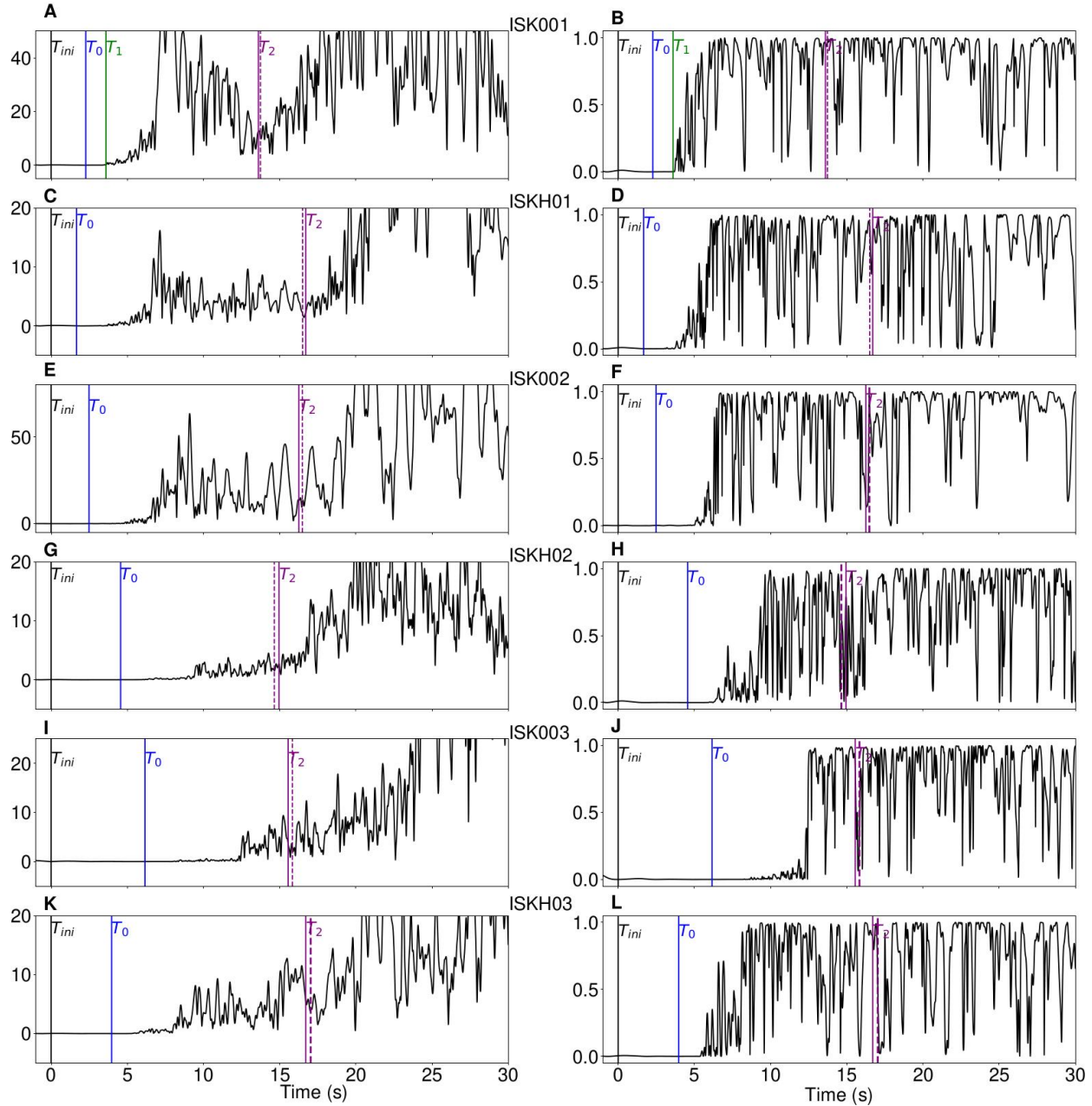


Fig. S11. Time-series waveforms for S arrival picking validation. (A) $[(\text{Ae}^2 + \text{An}^2 + \text{Au}^2)^{0.5}]$, where Ae is the East-West velocity seismogram, An is the North-South velocity seismogram, and Au is the Up-Down velocity seismogram at station ISK001. (B) $[(\text{Ae}^2 + \text{An}^2) / (\text{Ae}^2 + \text{An}^2 + \text{Au}^2 + 0.0001 * \max(\text{Ae}^2 + \text{An}^2 + \text{Au}^2))]$ at station ISK001. T_{ini} indicates the earthquake starting time, according to JMA catalog. T_0 is the manually picked P arrival. T_1 is the manually picked beginning of the first wave group. T_2 with the solid line is the manually picked S arrival in the second wave group. The dashed purple line is the predicted S arrival time based on the best-fit second hypocenter location. (C,D) The same as (A,B) but for station ISKH01. (E,F) The same as (A,B) but for station ISK002. (G,H) The same as (A,B) but for station ISKH02. (I,J) The same as (A,B) but for station ISK003. (K,L) The same as (A,B) but for station ISKH03.

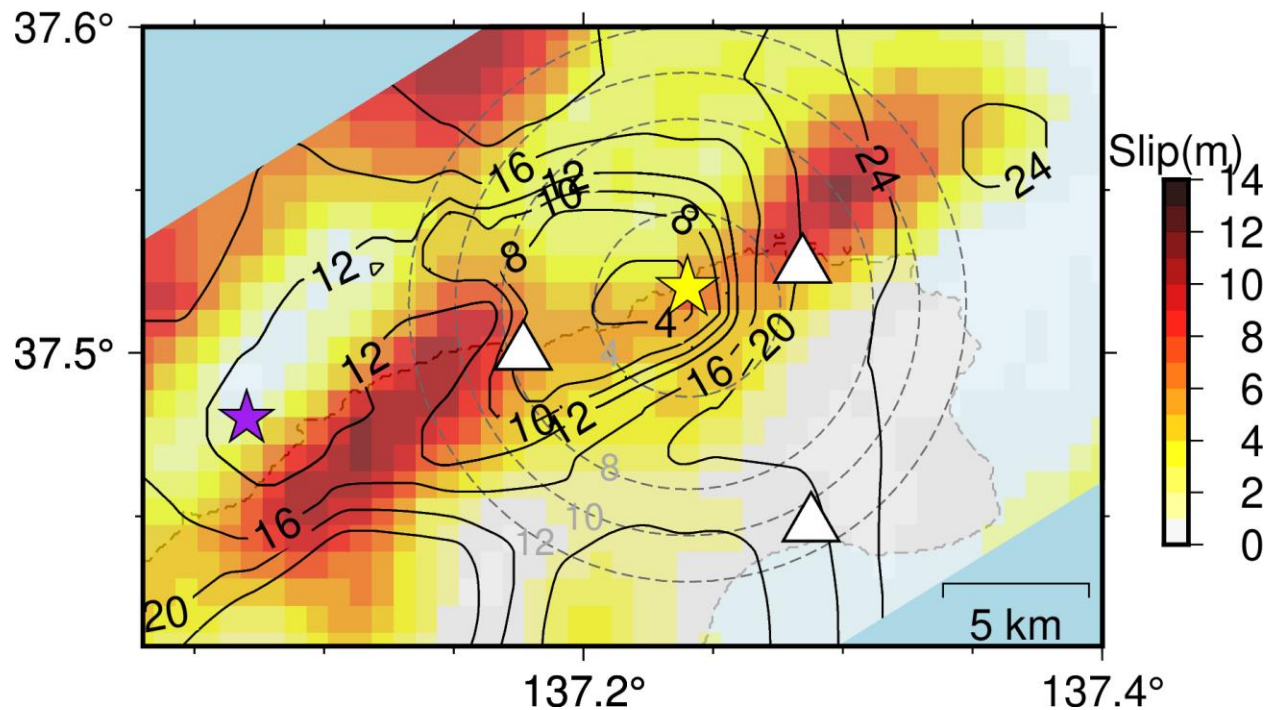


Fig. S12. Comparison of the early southwest rupture resolved by FFI and SEBP. The black contours with numbers indicate the rupture time in seconds resolved by FFI. The gray dashed contours and numbers indicate the rupture fronts propagating by 0.79 km/s, at 4 s, 8 s, 10 s, and 12 s, from inside (the hypocenter) to outside. The southwest rupture speed measured by SEBP is 0.79 km/s.

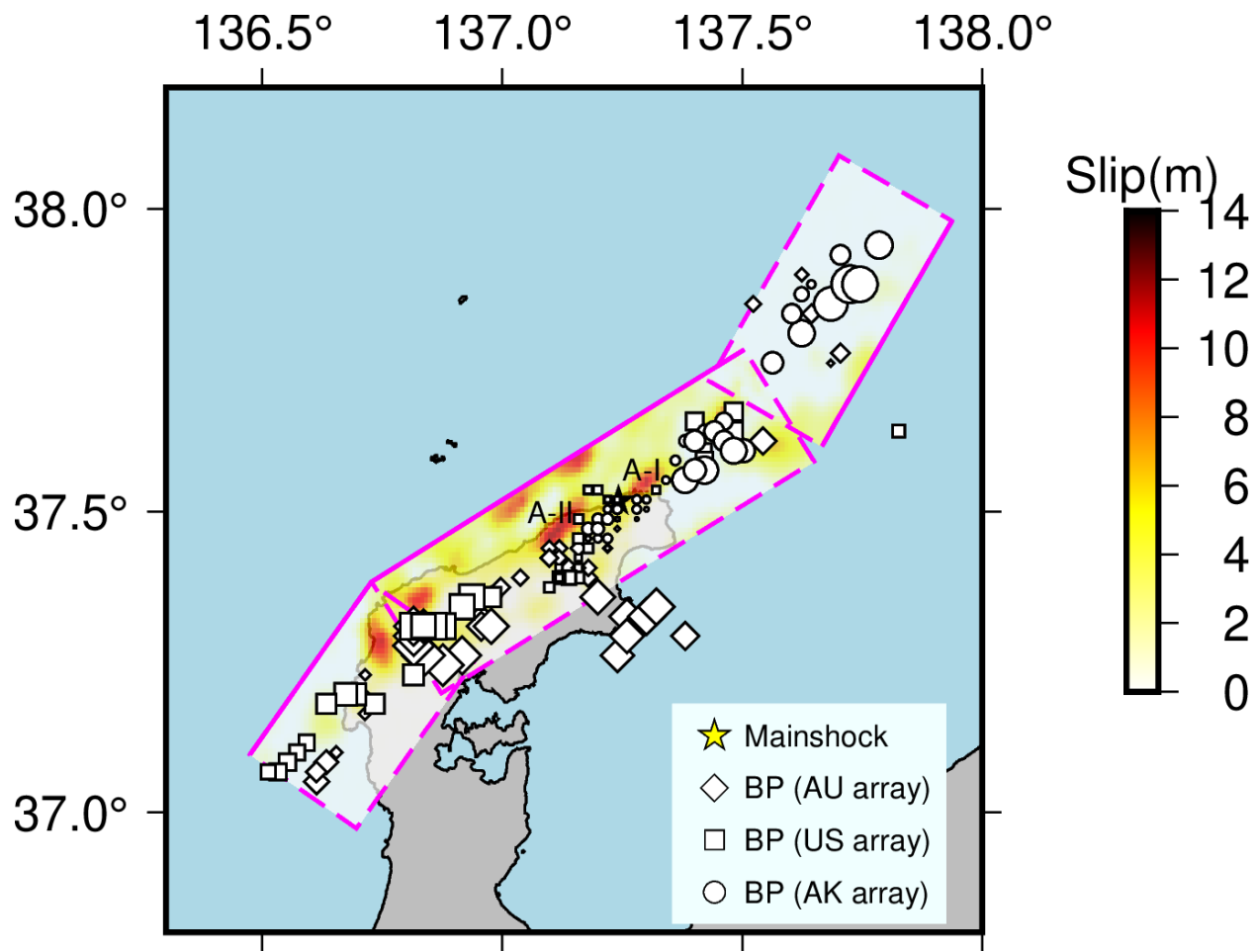


Fig. S13. High-frequency (HF) radiators and the coseismic slip model. Symbols indicate the location of HF radiators resolved by the Alaska (AK) array (white circles), the Australia (AU) array (white diamonds) and the USArray (white squares). The solid magenta lines denote upper boundaries of the fault planes. The colormap indicates the spatial distribution of the coseismic slip.

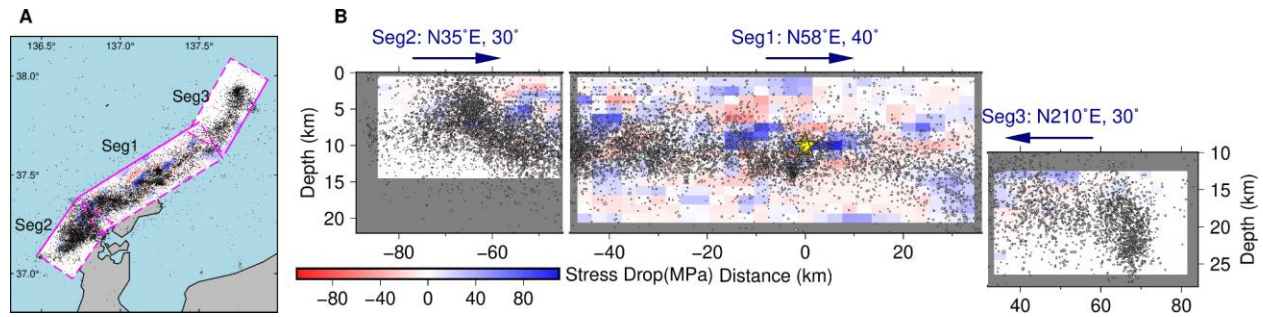
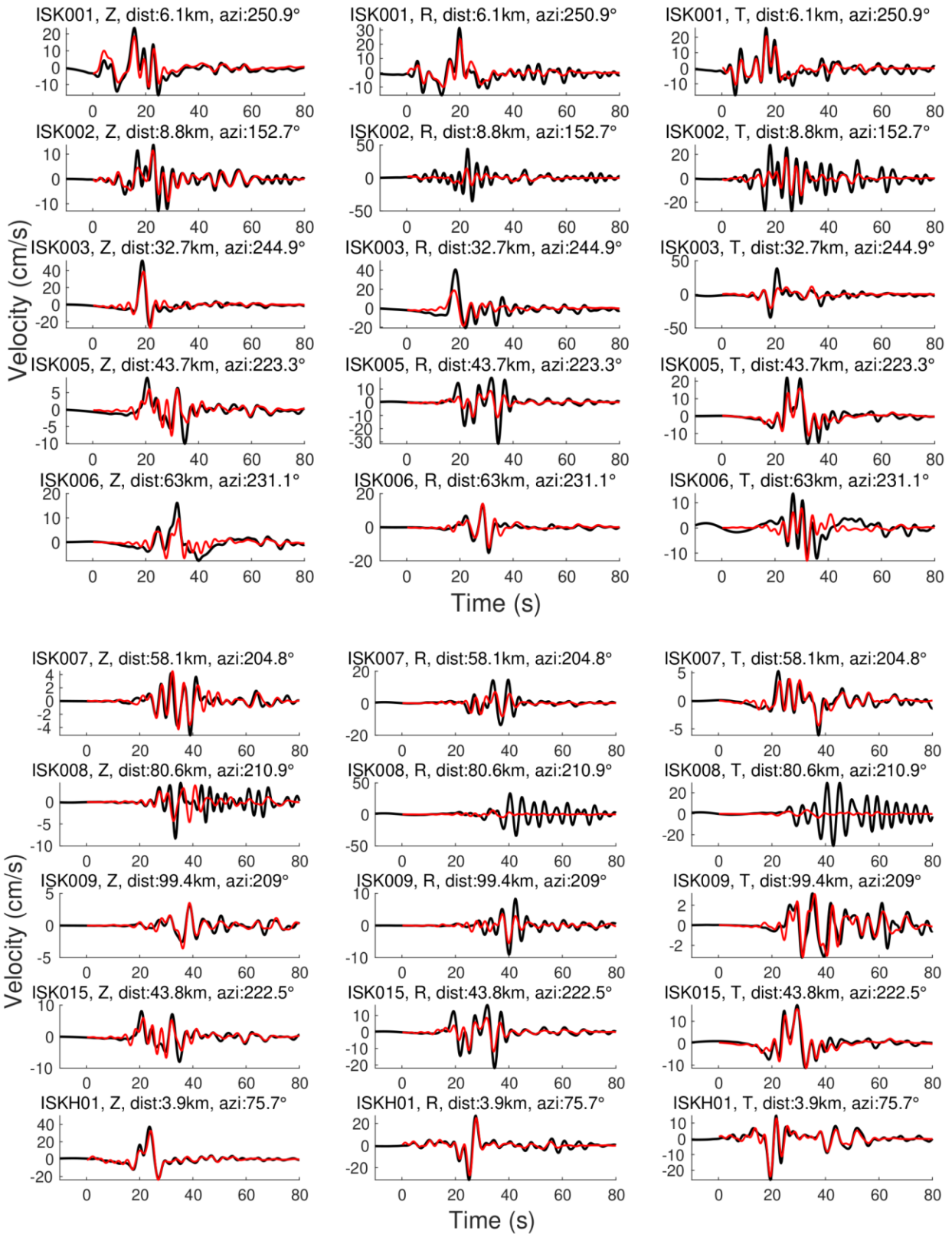


Fig. S14. Static stress drop in 112° rake angle. Positive values indicate stress drop and negative values indicate the stress increase. (A) The map view of stress drop and aftershocks distribution. The gray dots denote aftershocks that occurred between Jan 1st and 24th, 2024, from the JMA catalog. (B) Cross-section view of the stress drop and aftershocks.



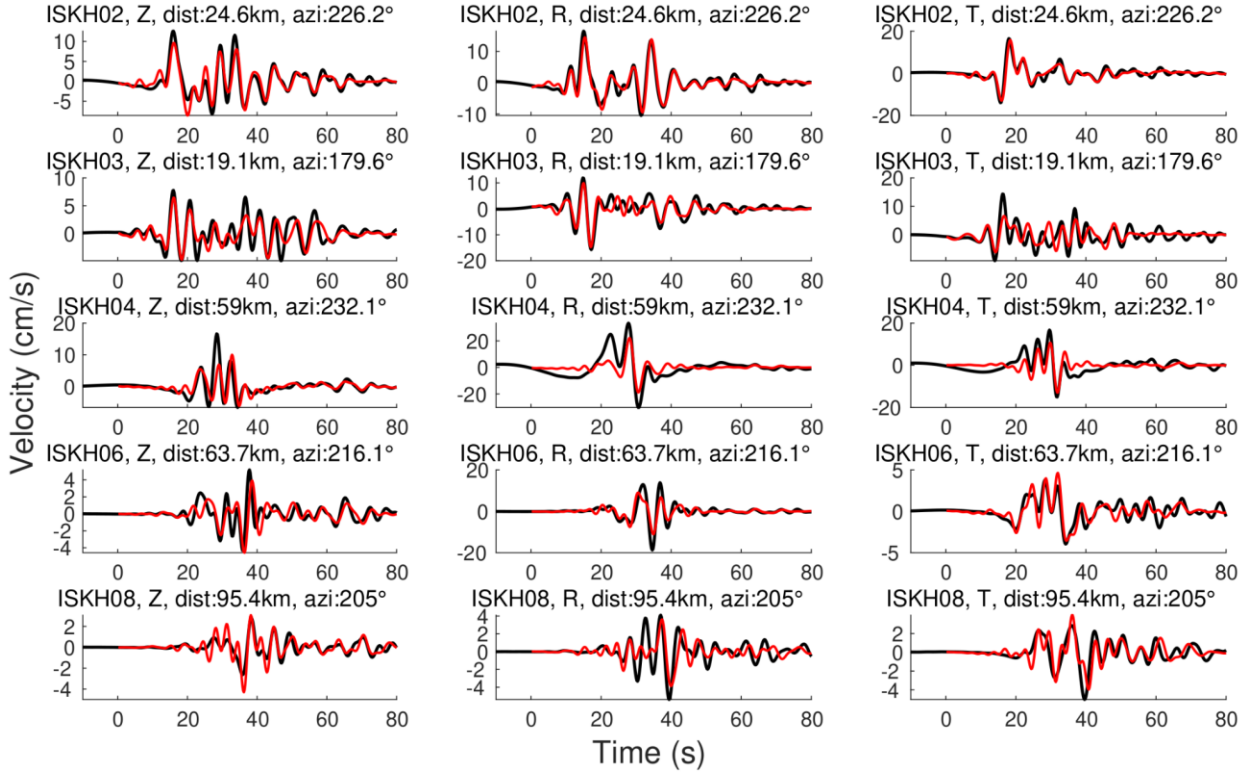
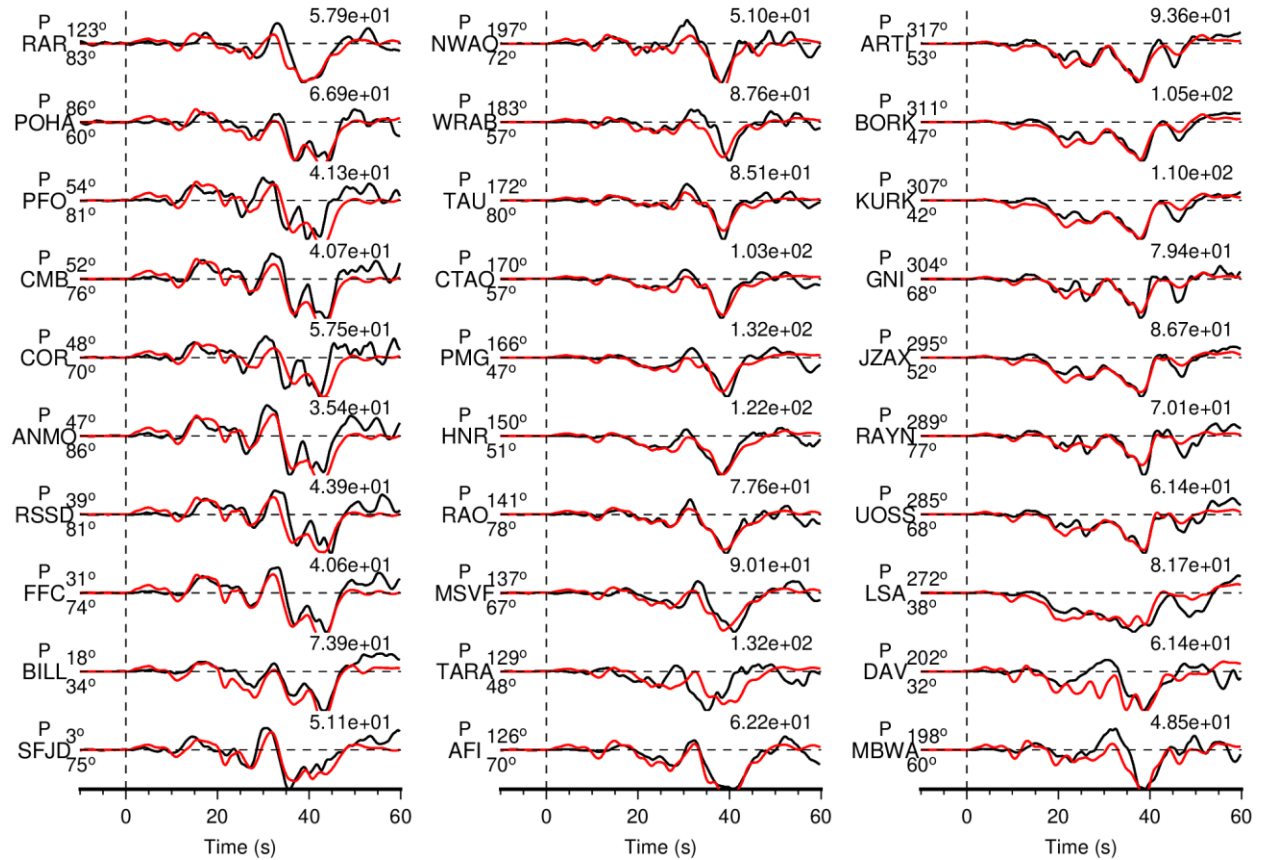


Fig. S15. Comparison between observed near-field strong motion station waveforms (black lines) and synthetic seismograms (red lines). The component (Z: vertical; R: radial; T: transverse) and the station name are shown at the top of each trace, accompanied by azimuth in degree and epicenter distance in km. The unit of velocity waveforms is cm/s.



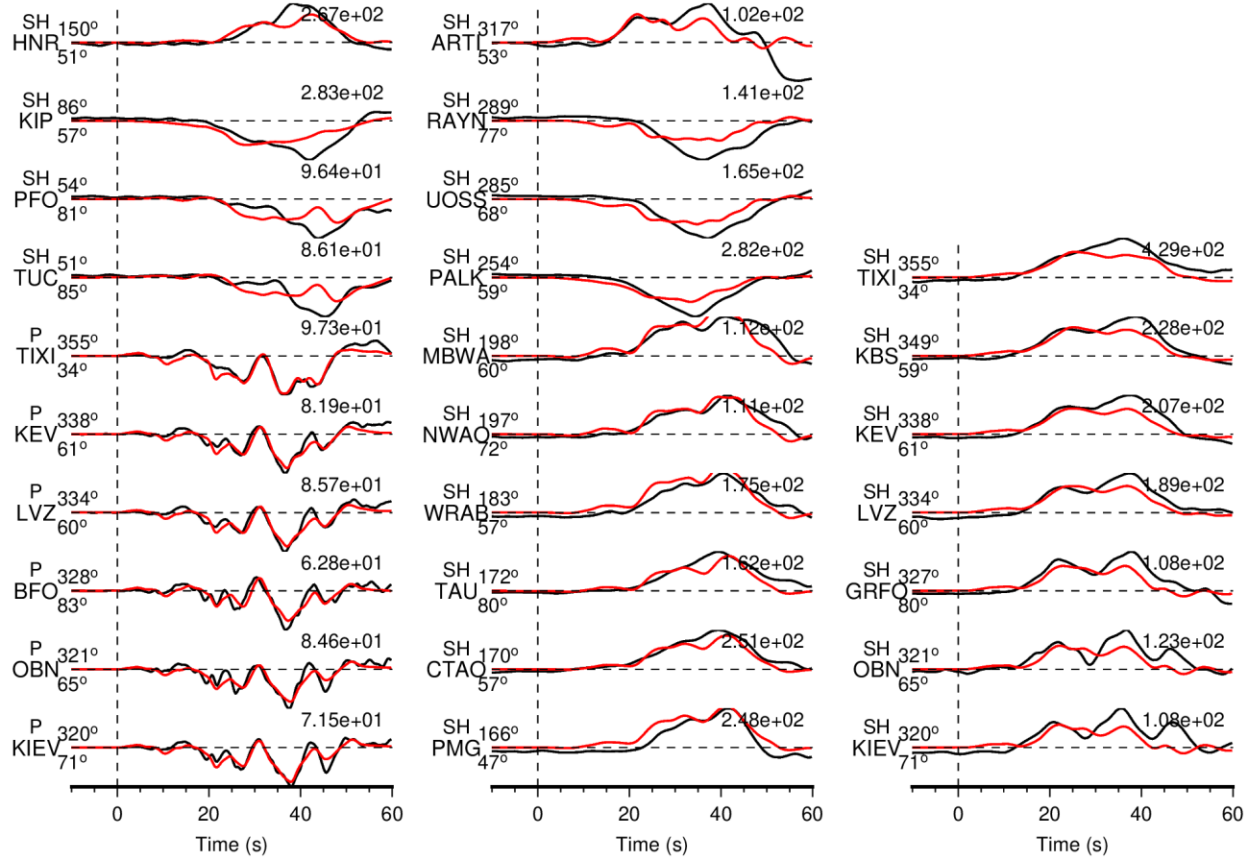


Fig. S16. Comparison between observed teleseismic broadband body wave waveforms (black lines) and synthetic seismograms (red lines) generated by the preferred model of the Mw 7.5 event. The wave type and the station name are shown to the left of each trace, along with azimuth (upper) and epicenter distance (lower) in degrees. The observed peak displacement in 10^{-6} m is denoted above the end of each trace.

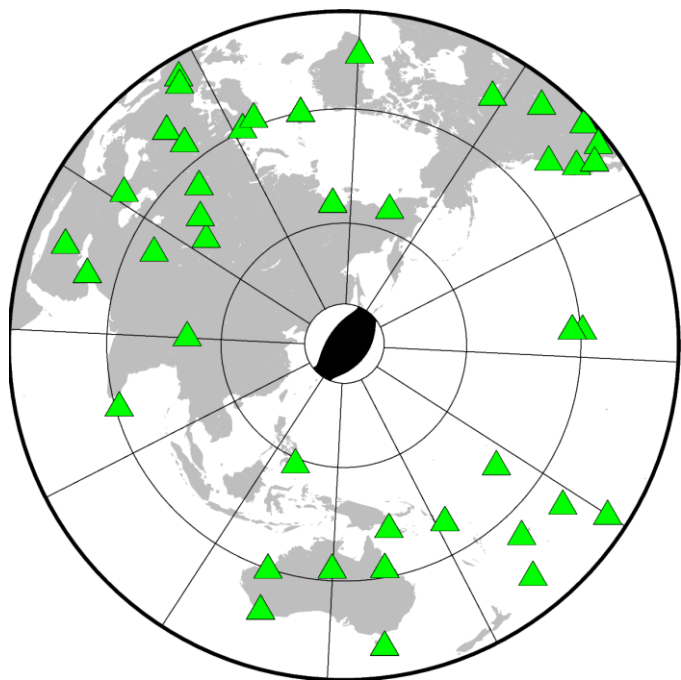
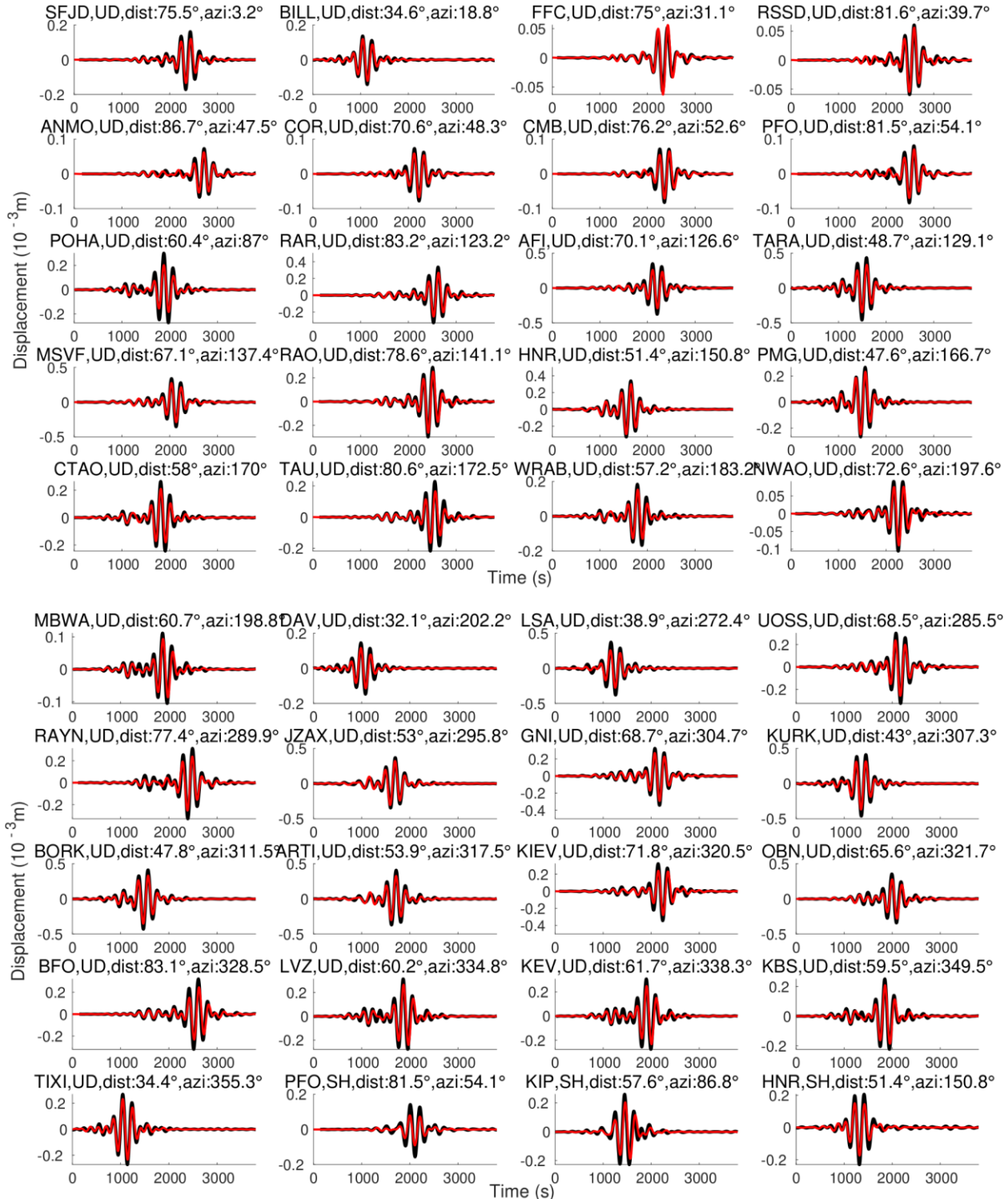


Fig. S17. Teleseismic stations recording broad-band body waves used in the joint FFI.



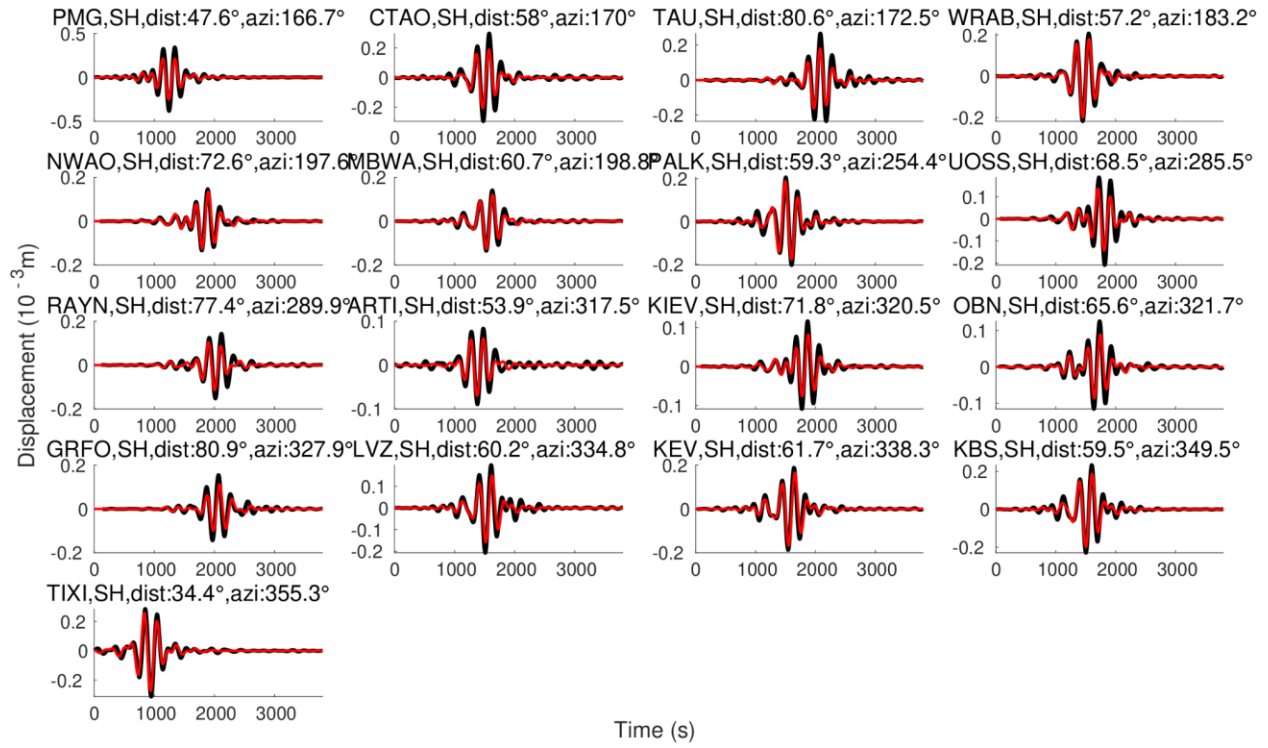


Fig. S18. Comparison between observed teleseismic long-period surface wave waveforms (black lines) and synthetic seismograms (red lines) generated by the preferred model of the Mw 7.5 event. The wave type and the station name are shown at the top of each trace, along with azimuth and epicenter distance in degree.

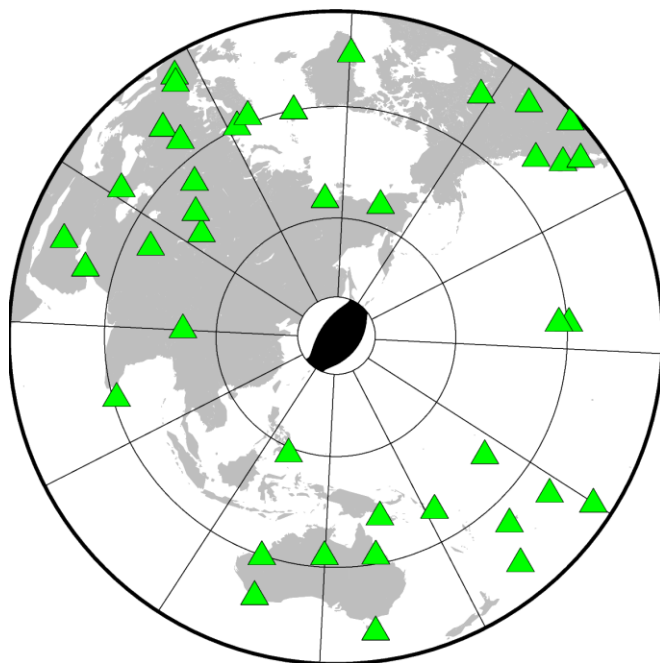


Fig. S19. Teleseismic stations recording long-period surface waves used in the joint FFI.

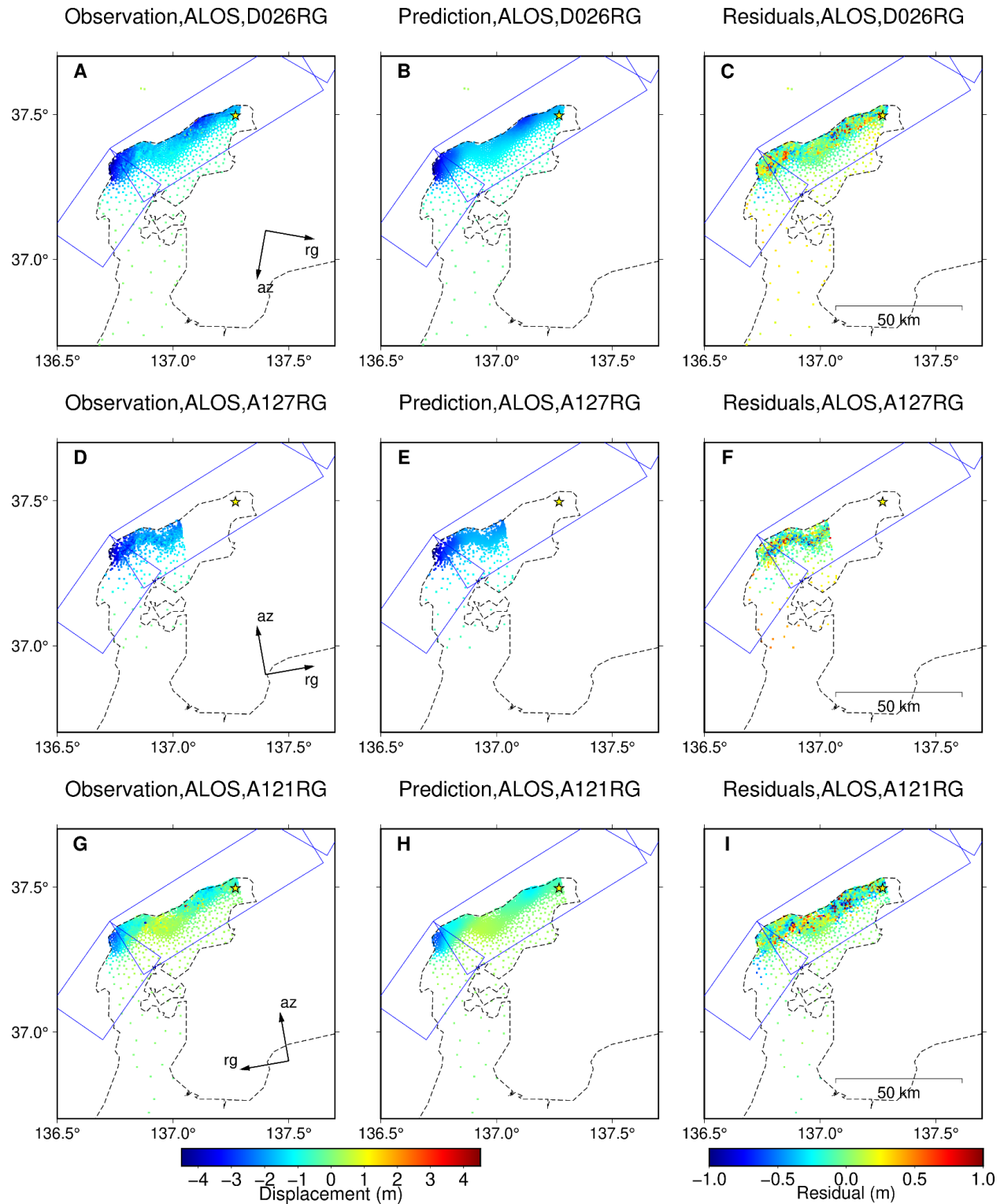


Fig. S20. The sub-sampled SAR data fits. The first column is the resampled static displacement (observation). The second column is the prediction by the preferred model. The third column is the residuals obtained by deducting the prediction from the observation. Blue boxes denote the fault planes adopted in joint finite fault inversion.

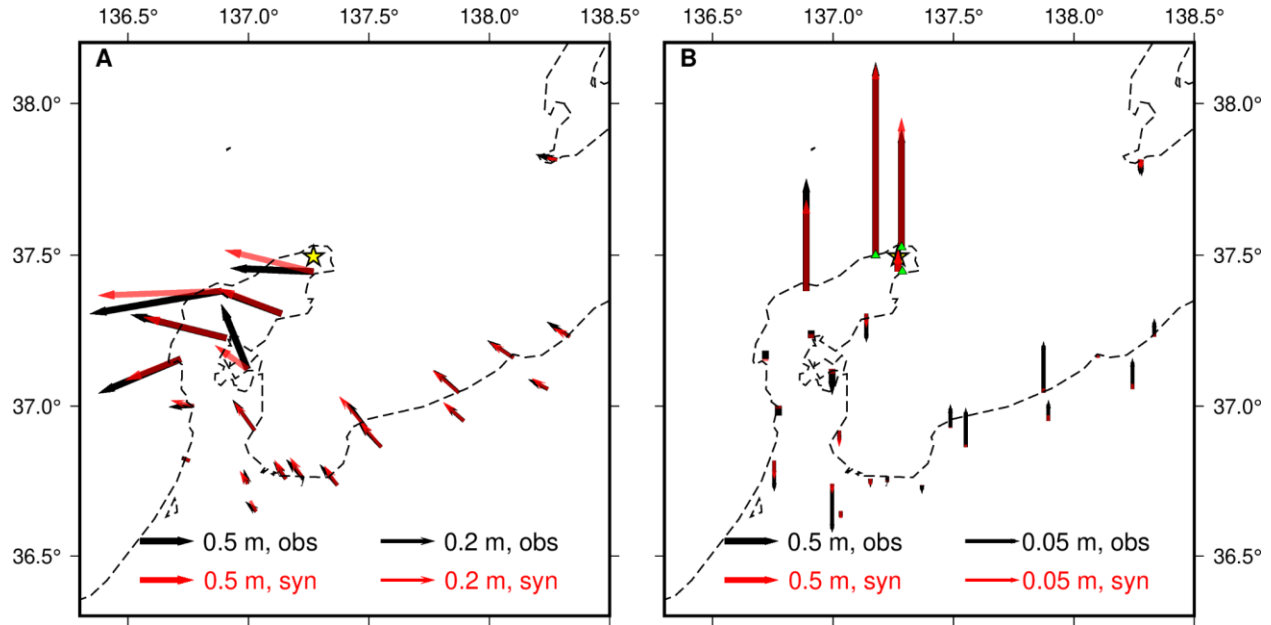


Fig. S21. Observed and synthetic ground displacements at near field GNSS and strong motion stations. The observations are denoted by black arrows and the syntheses are denoted by red arrows. (A) Lateral displacements recorded by GNSS stations. The displacements with amplitudes of ≥ 0.2 m are indicated with bold arrows, and the displacements with amplitudes of < 0.2 m are indicated with thin arrows. (B) Vertical displacements recorded by GNSS stations and obtained by integrating recordings at three strong motion stations. The displacements with amplitudes of ≥ 0.05 m are indicated with bold arrows, and the displacements with amplitudes of < 0.05 m are indicated with thin arrows. Vertical components of the acceleration seismograms from three strong motion stations (ISK001, ISK002, ISKH01; green triangles) are integrated and drift-removed (21), then also included in the inversion.

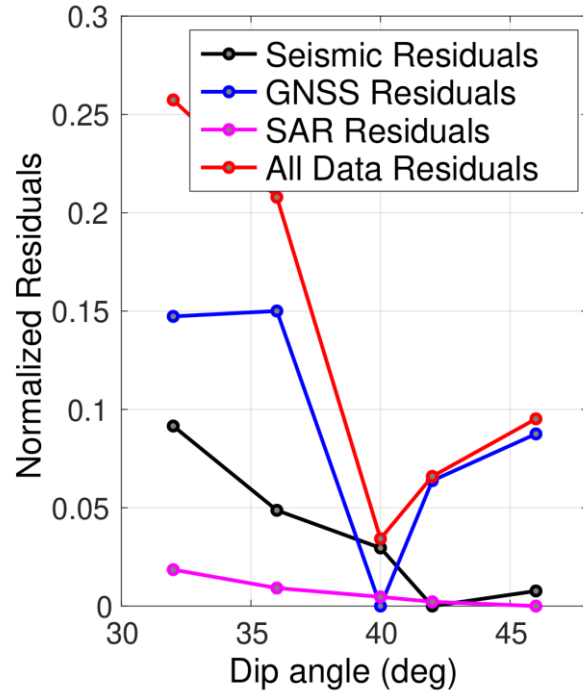


Fig. S22. The normalized residuals of slip models with different dip angles of segment 1. Note that “All Data Residuals” = “Seismic Residuals” + “GNSS Residuals” + “SAR Residuals”.

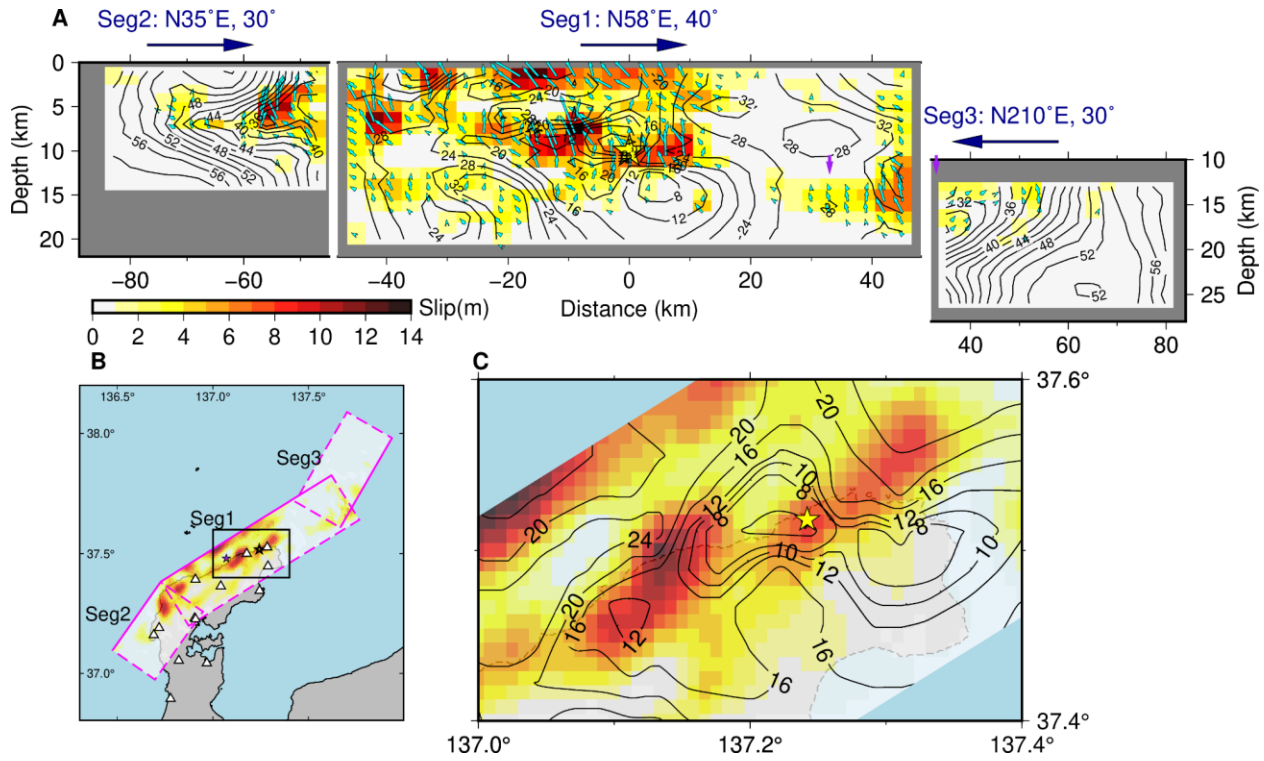


Fig. S23. Finite Fault Inversion (FFI) results of the model with an extended segment 1. (A) Spatial distribution of final slip (colors), rupture initiation time (contours), and slip direction (rake angle, cyan arrows) along the fault system. Top labels indicate the orientation (strike angle) and dip angle of each fault segment. The purple arrows indicate the connecting location of segments 1 and 3. (B) Map view of the slip and fault geometry model. (C) Sketch of the early rupture stage.

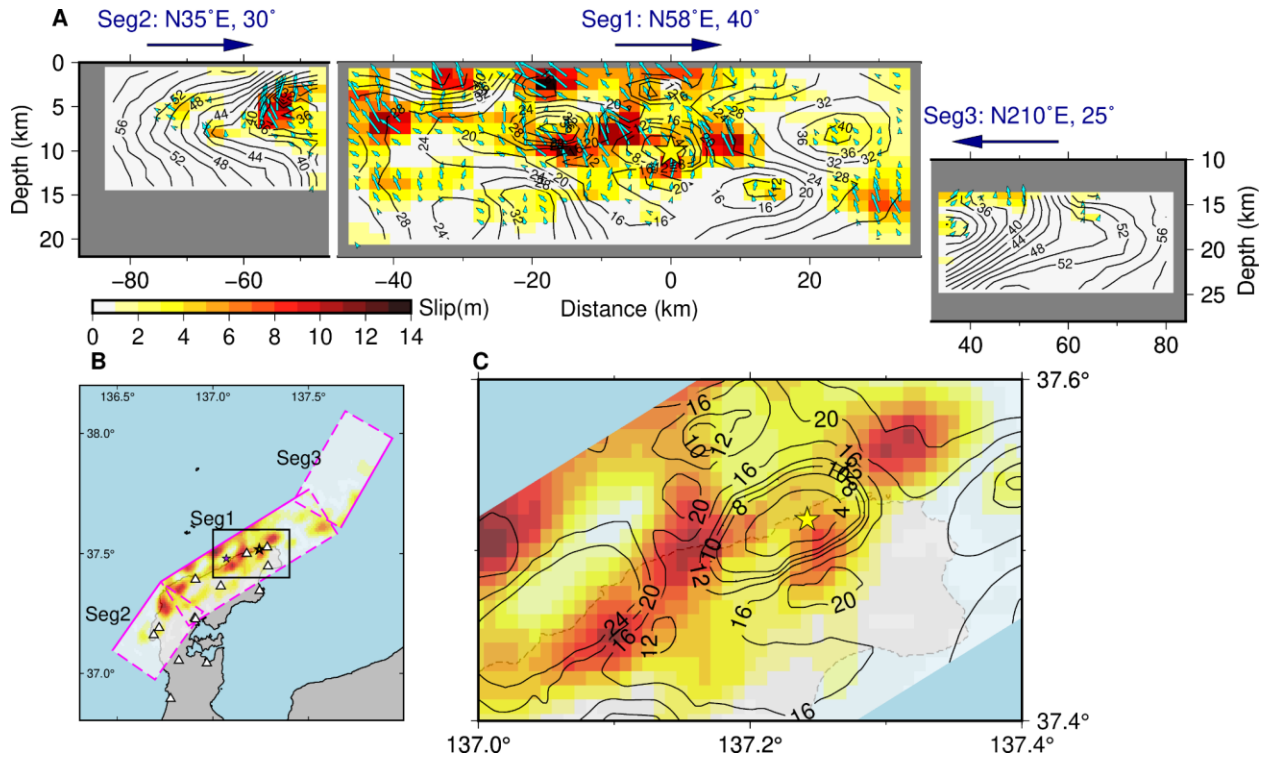


Fig. S24. Finite Fault Inversion (FFI) results of the model with a flatter segment 3. (A) Spatial distribution of final slip (colors), rupture initiation time (contours), and slip direction (rake angle, cyan arrows) along the fault system. Top labels indicate the orientation (strike angle) and dip angle of each fault segment. (B) Map view of the slip and fault geometry model. (C) Sketch of the early rupture stage.

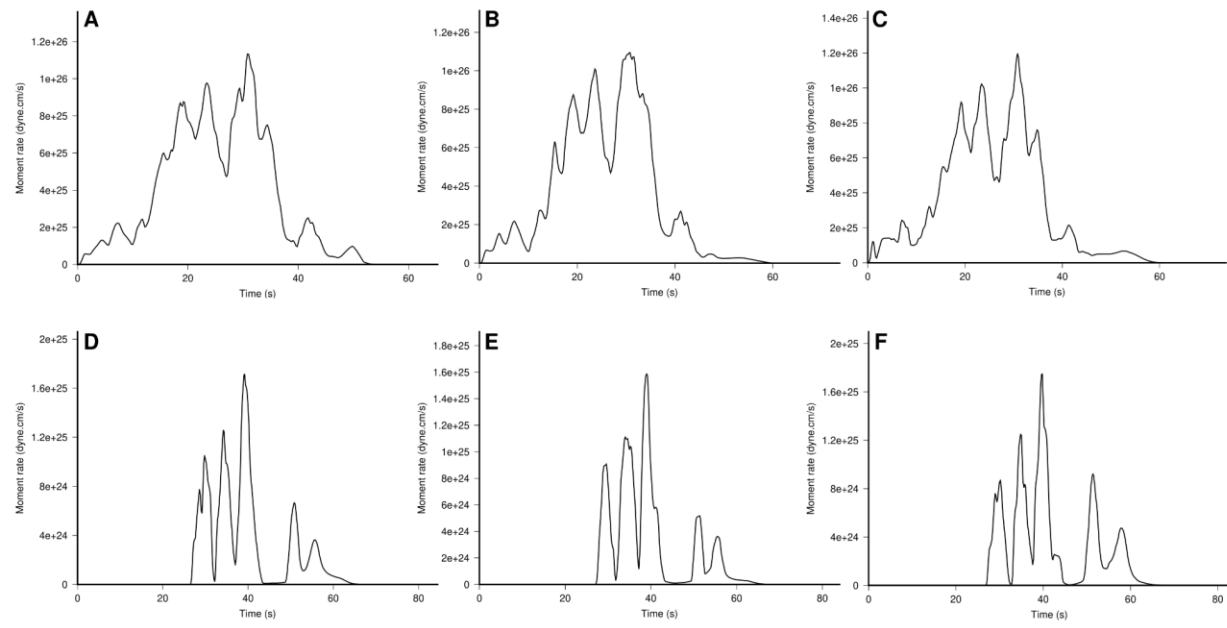


Fig. S25. The moment rate functions of the preferred model (A, D), the extended-segment-1 model (B, E), and the flatter-segment-3 model (C, F) on segment 1 (A, B, C) and segment 3 (D, E, F).

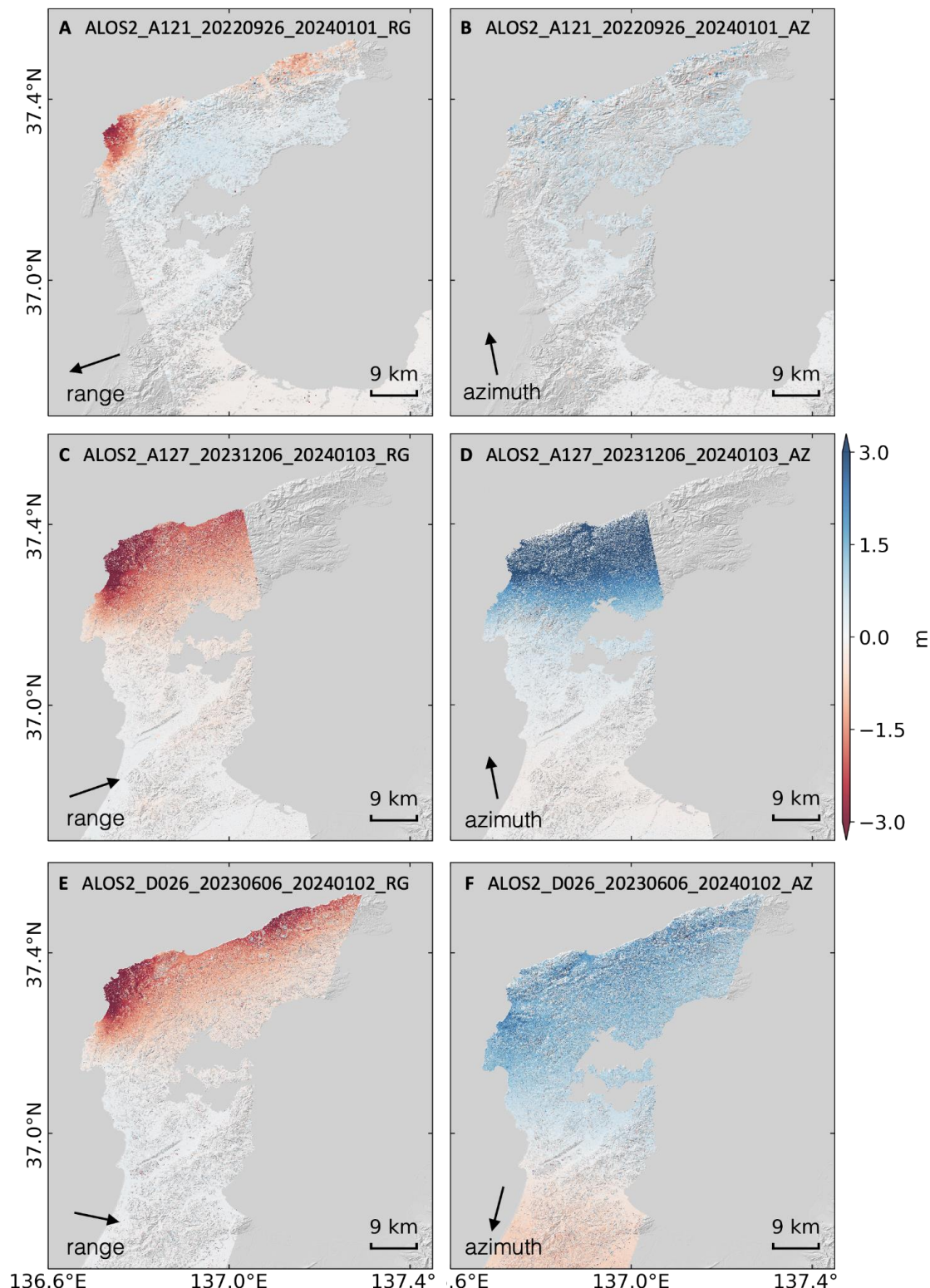


Fig. S26. The original resolution displacement data from the L-band ALOS-2 satellite. (A-B) ALOS-2 ascending track 121 offsets in slant range and ground azimuth directions, respectively. (C-D) Same as (A-B) but for ALOS-2 ascending track 127. (E-F) Same as (A-B) but for ALOS-2

descending track 26. Due to the potentially strong impact of the ionosphere, the three azimuth offsets are not used in the finite fault inversion.

Table S1. Hypocenter 2 locations resolved by the finite fault inversions with different dip angles of segment 1.

Dip angle (°)	Latitude (°N)	Longitude (°E)	Depth (km)	Time (s)
46	37.478	137.073	5.75	10.77
42	37.458	137.089	8.73	10.49
40	37.470	137.079	7.50	10.75
36	37.459	137.088	8.89	10.69
32	37.472	137.077	7.95	10.55

Table S2. The coordinates of the aftershocks used to calibrate the BP results. The time and coordinates of the aftershocks from the JMA catalog are shown on the left (accessed on Jan 5, 2024). The results of the aftershock locations before and after slowness calibration are shown along with their distance errors and root-mean-square error relative to the location in the JMA catalog. (A) shows the results of the AK array BP, (B) shows the results of the AU array BP, (C) shows the results of the EU array BP, and (D) shows the results of the USArray BP.

(A) AK array BP.

The JMA catalog			Before calibration			After calibration		
Time (JMA)	Lat	Lon	Lat	Lon	Distance error (km)	Lat	Lon	Distance error (km)
2024-01-01 16:06:06	37.511	137.246	37.51	137.23	1.42	37.51	137.24	0.54
2024-01-01 18:03:50	37.593	137.408	37.61	137.42	2.17	37.59	137.4	0.78
2024-01-01 19:06:56	37.886	137.711	38.05	137.74	18.41	37.93	137.72	4.96
RMS error (km)					10.73			

(B) AU array BP.

The JMA catalog			Before calibration			After calibration		
Time (JMA)	Lat	Lon	Lat	Lon	Distance error (km)	Lat	Lon	Distance error (km)
2023-05-05 14:42:04	37.539	137.304	37.54	137.36	4.94	37.54	137.3	0.37
2024-01-01 18:03:50	37.593	137.408	37.62	137.48	7.02	37.6	137.42	1.31

2024-01-04 17:16:25	37.713	137.526	37.78	137.62	11.13	37.74	137.54	3.24
2024-01-03 10:54:35	37.373	136.873	37.4	136.95	7.44	37.38	136.91	3.36
2024-01-01 16:56:49	37.262	136.857	37.28	136.87	2.31	37.26	136.85	0.66
2024-01-02 10:17:33	37.222	136.722	37.22	136.71	1.09	37.22	136.71	1.09
2024-01-02 4:42:07	37.257	136.677	37.26	136.65	2.41	37.26	136.65	2.41
RMS error (km)					6.16			2.11

(C) EU array BP.

The JMA catalog			Before calibration			After calibration		
Time (JMA)	Lat	Lon	Lat	Lon	Distance error (km)	Lat	Lon	Distance error (km)
2023-05-05 14:42:04	37.539	137.304	37.54	137.3	0.37	37.54	137.3	0.37
2024-01-01 18:03:50	37.593	137.408	37.62	137.42	3.18	37.6	137.42	1.31
2024-01-04 17:16:25	37.713	137.526	37.77	137.52	6.36	37.72	137.52	0.94
2024-01-01 19:06:56	37.886	137.711	38.07	137.76	20.91	37.97	137.72	9.37
2024-01-01 16:56:49	37.262	136.857	37.26	136.83	2.40	37.26	136.83	2.40
2024-01-02	37.222	136.722	37.22	136.69	2.84	37.22	136.71	1.09

10:17:33								
2024-01-02 4:42:07	37.257	136.677	37.28	136.69	2.80	37.26	136.69	1.18
RMS error (km)					8.53			3.76

(D) USArray BP.

The JMA catalog			Before calibration			After calibration		
Time (JMA)	Lat	Lon	Lat	Lon	Distance error (km)	Lat	Lon	Distance error (km)
2023-05-05 14:42:04	37.539	137.304	37.56	137.36	5.46	37.54	137.3	0.37
2024-01-01 18:03:50	37.593	137.408	37.58	137.44	3.17	37.57	137.4	2.65
2024-01-03 10:54:35	37.373	136.873	37.36	136.81	5.75	37.38	136.85	2.18
2024-01-01 16:56:49	37.262	136.857	37.18	136.81	10.02	37.24	136.85	2.52
2024-01-02 10:17:33	37.222	136.722	37.12	136.67	12.24	37.2	136.71	2.67
2024-01-02 4:42:07	37.257	136.677	37.14	136.61	14.30	37.18	136.67	8.58
RMS error (km)					9.38			4.06

Table S3. Weights of all datasets used in the joint finite fault inversion. *: some strong motion stations have higher weights than other stations, and the weight for each station can be found in the “SM.inf” file in the Zenodo folder (53).

Datasets	Weights
Teleseismic P wave	1
Teleseismic S wave	0.5
Teleseismic Rayleigh wave	4
Teleseismic Love wave	8
SAR	1
GNSS	1
Strong motion *	1

Table S4. Parameters used in the preferred model of joint finite fault inversion.

Segment 1		Segment 2		Segment 3	
Strike (°)	58	Strike (°)	35	Strike (°)	210
Dip (°)	40	Dip (°)	30	Dip (°)	30
Length (km)	81	Length (km)	39	Length (km)	48
Width (km)	32	Width (km)	28	Width (km)	28
Position of the top-east corner (lon, lat, depth)	136.728 E, 37.384 N, 0.557 km.	Position of the top-east corner	136.475 E, 37.097 N, 0.528 km.	Position of the top-east corner	137.666 E, 37.609 N, 12.955 km.

Table S5. The velocity model used in the joint finite fault inversion, adapted from (63).

Depth range (km)	Vp (km/s)	Vs (km/s)	Density (10^3kg/m^3)	Qp	Qs
0 - 1	4.5	2.1	2.48	400	200
1 - 5	5.5	3.18	2.6	600	300
5 - 18	6.0	3.46	2.7	700	350
18 - 30	6.6	3.8	2.9	800	400
30 - 40	7.8	4.5	3.1	1000	500

Table S6. The picked T_2 at six near-source stations.

Stations	Manually picked T_2
T_2 _ISK001	13.6 s
T_2 _ISKH01	16.7 s
T_2 _ISK002	16.25 s
T_2 _ISKH02	14.95 s
T_2 _ISK003	15.55 s
T_2 _ISKH03	16.7 s

Table S7. Used synthetic aperture radar (SAR) image information.

Sensor (band)	Post- / pre-seismic Date	Track (Frame)	Orbit Direction	Beam Mode	Acquisition Time UTC (local time)
ALOS-2 (L-band)	2024-01-01 / 2022-09-26	121 (0750-0770)	Asc	U2-6L	14:10 (23:10)
	2024-01-03 / 2023-12-06	127 (0720-0730)	Asc	U2-9R	14:51 (23:51)
	2024-01-02 / 2023-06-06	026 (2820-2840)	Dsc	U2-8L	03:37 (12:37)

Captions for Supplementary Movies

Movie S1. The rupture process resolved by SEBP using the AK array. The white star denotes the hypocenter of the mainshock.

Movie S2. The rupture process resolved by SEBP using the AU array. The white star denotes the hypocenter of the mainshock.

Movie S3. The rupture process resolved by SEBP using the EU array. The white star denotes the hypocenter of the mainshock.

Movie S4. The rupture process resolved by SEBP using the US array. The white star denotes the hypocenter of the mainshock.

Movie S5. The snapshot showing the rupture propagation resolved by joint FFI.

References and Notes

1. L. Meng, J.-P. Ampuero, J. Stock, Z. Duputel, Y. Luo, V. C. Tsai, Earthquake in a maze: Compressional rupture branching during the 2012 M_w 8.6 Sumatra earthquake. *Science* **337**, 724–726 (2012). [doi:10.1126/science.1224030](https://doi.org/10.1126/science.1224030) [Medline](#)
2. L. Xu, S. Mohanna, L. Meng, C. Ji, J.-P. Ampuero, Z. Yunjun, M. Hasnain, R. Chu, C. Liang, The overall-subshear and multi-segment rupture of the 2023 Mw7.8 Kahramanmaraş, Turkey earthquake in millennia supercycle. *Commun. Earth Environ.* **4**, 379 (2023). [doi:10.1038/s43247-023-01030-x](https://doi.org/10.1038/s43247-023-01030-x)
3. K. Aki, Asperities, barriers, characteristic earthquakes and strong motion prediction. *J. Geophys. Res.* **89**, 5867–5872 (1984). [doi:10.1029/JB089iB07p05867](https://doi.org/10.1029/JB089iB07p05867)
4. E. E. Brodsky, J. D. Kirkpatrick, T. Candela, Constraints from fault roughness on the scale-dependent strength of rocks. *Geology* **44**, 19–22 (2016). [doi:10.1130/G37206.1](https://doi.org/10.1130/G37206.1)
5. O. Zielke, M. Galis, P. M. Mai, Fault roughness and strength heterogeneity control earthquake size and stress drop. *Geophys. Res. Lett.* **44**, 777–783 (2017). [doi:10.1002/2016GL071700](https://doi.org/10.1002/2016GL071700)
6. S. Toda, R. S. Stein, “Intense seismic swarm punctuated by a magnitude 7.5 Japan shock,” *Temblor*, 4 January 2024; <https://doi.org/10.32858/temblor.333>
7. L. Jolivet, K. Tamaki, M. Fournier, Japan Sea, opening history and mechanism: A synthesis. *J. Geophys. Res.* **99**, 22237–22259 (1994). [doi:10.1029/93JB03463](https://doi.org/10.1029/93JB03463)
8. Y. Amezawa, Y. Hiramatsu, A. Miyakawa, K. Imanishi, M. Otsubo, Long-living earthquake swarm and intermittent seismicity in the northeastern tip of the Noto Peninsula, Japan. *Geophys. Res. Lett.* **50**, e2022GL102670 (2023). [doi:10.1029/2022GL102670](https://doi.org/10.1029/2022GL102670)
9. A. Kato, Implications of fault-valve behavior from immediate aftershocks following the 2023 M_j 6.5 earthquake beneath the Noto Peninsula, central Japan. *Geophys. Res. Lett.* **51**, e2023GL106444 (2024). [doi:10.1029/2023GL106444](https://doi.org/10.1029/2023GL106444)
10. J. Nakajima, Crustal structure beneath earthquake swarm in the Noto peninsula, Japan. *Earth Planets Space* **74**, 160 (2022). [doi:10.1186/s40623-022-01719-x](https://doi.org/10.1186/s40623-022-01719-x)
11. K. Yoshida, N. Uchida, Y. Matsumoto, M. Orimo, T. Okada, S. Hirahara, S. Kimura, R. Hino, Updip fluid flow in the crust of the northeastern Noto Peninsula, Japan, triggered the 2023 M_w 6.2 Suza earthquake during swarm activity. *Geophys. Res. Lett.* **50**, e2023GL106023 (2023). [doi:10.1029/2023GL106023](https://doi.org/10.1029/2023GL106023)
12. K. Yoshida, M. Uno, T. Matsuzawa, Y. Yukutake, Y. Mukuhira, H. Sato, T. Yoshida, Upward earthquake swarm migration in the northeastern Noto Peninsula, Japan, initiated from a deep ring-shaped cluster: Possibility of fluid leakage from a hidden magma system. *J. Geophys. Res. Solid Earth* **128**, e2022JB026047 (2023). [doi:10.1029/2022JB026047](https://doi.org/10.1029/2022JB026047)
13. T. Nishimura, Y. Hiramatsu, Y. Ohta, Episodic transient deformation revealed by the analysis of multiple GNSS networks in the Noto Peninsula, central Japan. *Sci. Rep.* **13**, 8381 (2023). [doi:10.1038/s41598-023-35459-z](https://doi.org/10.1038/s41598-023-35459-z) [Medline](#)

14. L. Meng, A. Zhang, Y. Yagi, Improving back projection imaging with a novel physics-based aftershock calibration approach: A case study of the 2015 Gorkha earthquake. *Geophys. Res. Lett.* **43**, 628–636 (2016). [doi:10.1002/2015GL067034](https://doi.org/10.1002/2015GL067034)
15. A. Zhang, “Theories and applications of enhanced earthquake back-projection imaging,” dissertation, University of California, 2019.
16. C. Ji, D. J. Wald, D. V. Helmberger, Source description of the 1999 Hector Mine, California, earthquake, Part I: Wavelet domain inversion theory and resolution analysis. *Bull. Seismol. Soc. Am.* **92**, 1192–1207 (2002). [doi:10.1785/0120000916](https://doi.org/10.1785/0120000916)
17. C. Ji, D. V. Helmberger, D. J. Wald, K.-F. Ma, Slip history and dynamic implications of the 1999 Chi-Chi, Taiwan, earthquake. *J. Geophys. Res.* **108**, 2412 (2003). [doi:10.1029/2002JB001764](https://doi.org/10.1029/2002JB001764)
18. Materials and methods are available as supplementary materials.
19. G. P. Hayes, The finite, kinematic rupture properties of great-sized earthquakes since 1990. *Earth Planet. Sci. Lett.* **468**, 94–100 (2017). [doi:10.1016/j.epsl.2017.04.003](https://doi.org/10.1016/j.epsl.2017.04.003)
20. M. Leonard, Earthquake fault scaling: Self-consistent relating of rupture length, width, average displacement, and moment release. *Bull. Seismol. Soc. Am.* **100**, 1971–1988 (2010). [doi:10.1785/0120090189](https://doi.org/10.1785/0120090189)
21. D. M. Boore, Effect of baseline corrections on displacements and response spectra for several recordings of the 1999 Chi-Chi, Taiwan, earthquake. *Bull. Seismol. Soc. Am.* **91**, 1199–1211 (2001). [doi:10.1785/0120000703](https://doi.org/10.1785/0120000703)
22. T. Lay, H. Kanamori, C. J. Ammon, K. D. Koper, A. R. Hutko, L. Ye, H. Yue, T. M. Rushing, Depth-varying rupture properties of subduction zone megathrust faults. *J. Geophys. Res.* **117**, B04311 (2012). [doi:10.1029/2011JB009133](https://doi.org/10.1029/2011JB009133)
23. P. Danré, D. Garagash, L. De Barros, F. Cappa, J.-P. Ampuero, Control of seismicity migration in earthquake swarms by injected fluid volume and aseismic crack propagation. *J. Geophys. Res. Solid Earth* **129**, e2023JB027276 (2024). [doi:10.1029/2023JB027276](https://doi.org/10.1029/2023JB027276)
24. W. L. Ellsworth, F. Bulut, Nucleation of the 1999 Izmit earthquake by a triggered cascade of foreshocks. *Nat. Geosci.* **11**, 531–535 (2018). [doi:10.1038/s41561-018-0145-1](https://doi.org/10.1038/s41561-018-0145-1)
25. E. M. Dunham, P. Favreau, J. M. Carlson, A supershear transition mechanism for cracks. *Science* **299**, 1557–1559 (2003). [doi:10.1126/science.1080650](https://doi.org/10.1126/science.1080650) Medline
26. K. Irikura, H. Miyake, Recipe for predicting strong ground motion from crustal earthquake scenarios. *Pure Appl. Geophys.* **168**, 85–104 (2011). [doi:10.1007/s00024-010-0150-9](https://doi.org/10.1007/s00024-010-0150-9)
27. H. Kanamori, E. E. Brodsky, The physics of earthquakes. *Rep. Prog. Phys.* **67**, 1429–1496 (2004). [doi:10.1088/0034-4885/67/8/R03](https://doi.org/10.1088/0034-4885/67/8/R03)
28. J. Li, T. Kim, N. Lapusta, E. Biondi, Z. Zhan, The break of earthquake asperities imaged by distributed acoustic sensing. *Nature* **620**, 800–806 (2023). [doi:10.1038/s41586-023-06227-w](https://doi.org/10.1038/s41586-023-06227-w) Medline
29. K. Umeda, K. Asamori, A. Makuuchi, K. Kobori, Y. Hama, Triggering of earthquake swarms following the 2011 Tohoku megathrust earthquake. *J. Geophys. Res. Solid Earth* **120**, 2279–2291 (2015). [doi:10.1002/2014JB011598](https://doi.org/10.1002/2014JB011598)

30. Z. E. Ross, E. S. Cochran, D. T. Trugman, J. D. Smith, 3D fault architecture controls the dynamism of earthquake swarms. *Science* **368**, 1357–1361 (2020).
[doi:10.1126/science.abb0779](https://doi.org/10.1126/science.abb0779) [Medline](#)
31. L. Wang, S. Xu, Y. Zhuo, P. Liu, S. Ma, Unraveling the roles of fault asperities over earthquake cycles. *Earth Planet. Sci. Lett.* **636**, 118711 (2024).
[doi:10.1016/j.epsl.2024.118711](https://doi.org/10.1016/j.epsl.2024.118711)
32. S. Lee, E. Choi, C. H. Scholz, Do subducted seamounts act as weak asperities? *J. Geophys. Res. Solid Earth* **128**, e2023JB027551 (2023). [doi:10.1029/2023JB027551](https://doi.org/10.1029/2023JB027551)
33. P. A. Selvadurai, S. D. Glaser, Laboratory-developed contact models controlling instability on frictional faults. *J. Geophys. Res. Solid Earth* **120**, 4208–4236 (2015).
[doi:10.1002/2014JB011690](https://doi.org/10.1002/2014JB011690)
34. P. A. Selvadurai, S. D. Glaser, Asperity generation and its relationship to seismicity on a planar fault: A laboratory simulation. *Geophys. J. Int.* **208**, 1009–1025 (2016).
[doi:10.1093/gji/ggw439](https://doi.org/10.1093/gji/ggw439)
35. T. Nishimura, Y. Yokota, K. Tadokoro, T. Ochi, Strain partitioning and interplate coupling along the northern margin of the Philippine Sea plate, estimated from Global Navigation Satellite System and Global Positioning System-Acoustic data. *Geosphere* **14**, 535–551 (2018). [doi:10.1130/GES01529.1](https://doi.org/10.1130/GES01529.1)
36. T. Usami, *Materials for Comprehensive List of Destructive Earthquakes in Japan [Latest Edition] [416]-2001* (Univ. Tokyo Press, 2003).
37. M. Hamada, Y. Hiramatsu, M. Oda, H. Yamaguchi, Fossil tubeworms link coastal uplift of the northern Noto Peninsula to rupture of the Wajima-oki fault in AD 1729. *Tectonophysics* **670**, 38–47 (2016). [doi:10.1016/j.tecto.2015.12.019](https://doi.org/10.1016/j.tecto.2015.12.019)
38. S. Ozawa, H. Yarai, M. Tobita, H. Une, T. Nishimura, Crustal deformation associated with the Noto Hanto Earthquake in 2007 in Japan. *Earth Planets Space* **60**, 95–98 (2008).
[doi:10.1186/BF03352767](https://doi.org/10.1186/BF03352767)
39. Y. Ota, K. Hirakawa, Marine terraces and their deformation in Noto Peninsula, Japan Sea side of central Japan [in Japanese with English abstract]. *Geogr. Rev. Jpn.* **52**, 169–189 (1979). [doi:10.4157/grj.52.169](https://doi.org/10.4157/grj.52.169)
40. M. Shishikura, T. Echigo, Y. Namegaya, Activity of marine active faults seen from the altitude distribution of low terraces and aquatic animal remains communities along the northern coast of the Noto Peninsula [in Japanese]. *Active Fault Research* **2020**, 33–49 (2020).
41. P. A. Rosen, E. Gurrola, G. F. Sacco, H. Zebker, “The InSAR scientific computing environment,” paper presented at EUSAR 2012, 23 to 26 April 2012, Nuremberg, Germany.
42. Z. Yunjun, yunjunz/2024-Noto-EQ: Version 1.0 (v1.0). Zenodo (2024);
<https://doi.org/10.5281/zenodo.12803386>.
43. L. Xu, L. Meng, Codes for slowness-enhanced back-projection (SEBP). Zenodo (2024);
<https://doi.org/10.5281/zenodo.12801968>.

44. U.S. Geological Survey, Earthquake Hazards Program, Advanced National Seismic System (ANSS) Comprehensive Catalog of Earthquake Events and Products: Various (2017); <https://doi.org/10.5066/F7MS3QZH>.
45. A. M. Dziewonski, T.-A. Chou, J. H. Woodhouse, Determination of earthquake source parameters from waveform data for studies of global and regional seismicity. *J. Geophys. Res.* **86**, 2825–2852 (1981). [doi:10.1029/JB086iB04p02825](https://doi.org/10.1029/JB086iB04p02825)
46. G. Ekström, M. Nettles, A. M. Dziewonski, The global CMT project 2004–2010: Centroid-moment tensors for 13,017 earthquakes. *Phys. Earth Planet. Inter.* **200-201**, 1–9 (2012). [doi:10.1016/j.pepi.2012.04.002](https://doi.org/10.1016/j.pepi.2012.04.002)
47. R. Newman, A. Clark, C. Trabant, R. Karstens, A. Hutko, R. Casey, T. Ahern, Wilber 3: A Python-Django web application for acquiring large-scale event-oriented seismic data (Incorporated Research Institutions for Seismology, 2013); <https://ds.iris.edu/wilber3/>.
48. A. Strollo, D. Cambaz, J. Clinton, P. Danecek, C. P. Evangelidis, A. Marmureanu, L. Ottemöller, H. Pedersen, R. Sleeman, K. Stammller, D. Armbruster, J. Bienkowski, K. Boukouras, P. L. Evans, M. Fares, C. Neagoe, S. Heimers, A. Heinloo, M. Hoffmann, P. Kaestli, V. Lauciani, J. Michalek, E. Odon Muhire, M. Ozer, L. Palangeanu, C. Pardo, J. Quinteros, M. Quintiliani, J. Antonio Jara-Salvador, J. Schaeffer, A. Schloemer, N. Triantafyllis, EIDA: The European Integrated Data Archive and Service Infrastructure within ORFEUS. *Seismol. Res. Lett.* **92**, 1788–1795 (2021). [doi:10.1785/0220200413](https://doi.org/10.1785/0220200413)
49. National Research Institute for Earth Science and Disaster Resilience, NIED K-NET, KiK-net, National Research Institute for Earth Science and Disaster Resilience. NIED Repository (2019); <https://doi.org/10.17598/NIED.0004>.
50. M. Beyreuther, R. Barsch, L. Krischer, T. Megies, Y. Behr, J. Wassermann, ObsPy: A Python toolbox for seismology. *Seismol. Res. Lett.* **81**, 530–533 (2010). [doi:10.1785/gssrl.81.3.530](https://doi.org/10.1785/gssrl.81.3.530)
51. P. Wessel, W. H. F. Smith, New, improved version of generic mapping tools released. *Eos* **79**, 579 (1998). [doi:10.1029/98EO00426](https://doi.org/10.1029/98EO00426)
52. R. B. Lohman, W. D. Barnhart, Evaluation of earthquake triggering during the 2005–2008 earthquake sequence on Qeshm Island, Iran. *J. Geophys. Res. Solid Earth* **115**, 12413 (2010).
53. L. Xu, Z. Yunjun, The results and datasets of 2024 Mw 7.5 Noto earthquake. Zenodo (2024); <https://doi.org/10.5281/zenodo.12786109>.
54. P. Koch, F. Bravo, S. Riquelme, J. G. F. Crempien, Near-real-time finite-fault inversions for large earthquakes in Chile using strong-motion data. *Seismol. Res. Lett.* **90**, 1971–1986 (2019). [doi:10.1785/0220180294](https://doi.org/10.1785/0220180294)
55. P. Bird, An updated digital model of plate boundaries. *Geochem. Geophys. Geosyst.* **4**, 1027 (2003). [doi:10.1029/2001GC000252](https://doi.org/10.1029/2001GC000252)
56. P. Shearer, *Introduction to Seismology* (Cambridge Univ. Press, ed. 2, 2009).
57. M. Ishii, P. M. Shearer, H. Houston, J. E. Vidale, Extent, duration and speed of the 2004 Sumatra-Andaman earthquake imaged by the Hi-Net array. *Nature* **435**, 933–936 (2005). [doi:10.1038/nature03675](https://doi.org/10.1038/nature03675) [Medline](#)

58. E. Kiser, M. Ishii, Back-projection imaging of earthquakes. *Annu. Rev. Earth Planet. Sci.* **45**, 271–299 (2017). [doi:10.1146/annurev-earth-063016-015801](https://doi.org/10.1146/annurev-earth-063016-015801)
59. L. Meng, A. Inbal, J. P. Ampuero, A window into the complexity of the dynamic rupture of the 2011 Mw 9 Tohoku-Oki earthquake. *Geophys. Res. Lett.* **38**, L00G07 (2011). [doi:10.1029/2011GL048118](https://doi.org/10.1029/2011GL048118)
60. M. K. Sen, P. L. Stoffa, Nonlinear one-dimensional seismic waveform inversion using simulated annealing. *Geophysics* **56**, 1624–1638 (1991). [doi:10.1190/1.1442973](https://doi.org/10.1190/1.1442973)
61. S. H. Hartzell, P. Liu, C. Mendoza, The 1994 Northridge, California, earthquake: Investigation of rupture velocity, rise time, and high-frequency radiation. *J. Geophys. Res.* **101**, 20091–20108 (1996). [doi:10.1029/96JB01883](https://doi.org/10.1029/96JB01883)
62. L. Zhu, L. A. Rivera, A note on the dynamic and static displacements from a point source in multilayered media. *Geophys. J. Int.* **148**, 619–627 (2002). [doi:10.1046/j.1365-246X.2002.01610.x](https://doi.org/10.1046/j.1365-246X.2002.01610.x)
63. K. Asano, T. Iwata, Source-Rupture Process of the 2007 Noto Hanto, Japan, Earthquake Estimated by the Joint Inversion of Strong Motion and GPS Data. *Bull. Seismol. Soc. Am.* **101**, 2467–2480 (2011). [doi:10.1785/0120100254](https://doi.org/10.1785/0120100254)
64. C. Liang, E. J. Fielding, Interferometry With ALOS-2 Full-Aperture ScanSAR Data. *IEEE Trans. Geosci. Remote Sens.* **55**, 2739–2750 (2017). [doi:10.1109/TGRS.2017.2653190](https://doi.org/10.1109/TGRS.2017.2653190)
65. European Space Agency, Copernicus Global Digital Elevation Model (2019); <https://doi.org/10.5270/ESA-c5d3d65> [accessed 14 January 2024].
66. G. Blewitt, W. Hammond, C. Kreemer, Harnessing the GPS data explosion for interdisciplinary science. *Eos* **99**, 1 (2018). [doi:10.1029/2018EO104623](https://doi.org/10.1029/2018EO104623)
67. W. Bertiger, Y. Bar-Sever, A. Dorsey, B. Haines, N. Harvey, D. Hemberger, M. Heflin, W. Lu, M. Miller, A. W. Moore, D. Murphy, P. Ries, L. Romans, A. Sibois, A. Sibthorpe, B. Szilagyi, M. Vallisneri, P. Willis, GipsyX/RTGx, a new tool set for space geodetic operations and research. *Adv. Space Res.* **66**, 469–489 (2020). [doi:10.1016/j.asr.2020.04.015](https://doi.org/10.1016/j.asr.2020.04.015)
68. Y. Okada, Internal deformation due to shear and tensile faults in a half-space. *Bull. Seismol. Soc. Am.* **82**, 1018–1040 (1992). [doi:10.1785/BSSA0820021018](https://doi.org/10.1785/BSSA0820021018)
69. J. Ripperger, P. M. Mai, Fast computation of static stress changes on 2D faults from final slip distributions. *Geophys. Res. Lett.* **31**, L18610 (2004). [doi:10.1029/2004GL020594](https://doi.org/10.1029/2004GL020594)